Decentralized Power Systems: Reference-Frame Theory and Stability Region Generation

by

Colm J. O'Rourke

B.E., Energy Systems Engineering
National University of Ireland, Galway (2013)
S.M., Electrical Engineering and Computer Science
Massachusetts Institute of Technology (2015)

Submitted to the Department of Electrical Engineering and Computer Science
in partial fulfillment of the requirements for the degree of

Doctor of Philosophy in Electrical Engineering and Computer Science

at the

MASSACHUSETTS INSTITUTE OF TECHNOLOGY

May 2020

Author .....
Department of Electrical Engineering and Computer Science
May 15, 2020

Certified by .....
James L. Kirtley
Professor of Electrical Engineering
Thesis Supervisor

Accepted by .....
Leslie A. Kolodziejski
Professor of Electrical Engineering and Computer Science
Chair, Department Committee on Graduate Students

Decentralized Power Systems: Reference-Frame Theory and Stability Region Generation

by

Colm J. O'Rourke

Submitted to the Department of Electrical Engineering and Computer Science
on May 15, 2020, in partial fulfillment of the
requirements for the degree of
Doctor of Philosophy in Electrical Engineering and Computer Science

Abstract

Electricity provides the foundation for many of today's technological advances. The desire for energy security, a reduction in carbon dioxide emissions and a diversification of resources are all motivations for changes in how electricity is generated and transmitted. Recent alternatives to traditional centralized power-plants include technologies that are decentralized and intermittent, such as solar photovoltaic and wind power. This trend poses considerable challenges in the hardware making up these systems, the software that control and monitor power networks and their mathematical modelling.

This thesis presents a set of contributions that address some of the aforementioned challenges. Firstly, we examine the fundamental theories used in modelling and controlling power systems. We expand previous work on reference-frame theory, by providing an alternative interpretation and derivation of the commonly used Park and Clarke transformations. We present a geometric interpretation that has applications in power quality. Secondly, we introduce a framework for producing regions of stability for power systems using conditional generative adversarial neural networks. This provides transmission and distribution operators with an accurate set of control options even as the system changes significantly.

Thesis Supervisor: James L. Kirtley
Title: Professor of Electrical Engineering

Acknowledgments

PhD theses are primarily an account and celebration of individual contributions to a field. In reality, we all learn from each other and no work is done in strict isolation. With this in mind, I have a few groups of people I would like to acknowledge in this work.

First and foremost my sincere thanks to my thesis supervisor Professor Kirtley. His patience and support was tremendously helpful in completing this research. He was always open to working on new problems including those not traditional to his research background. He gave me the freedom to grow and mature as a researcher and I am grateful to have had him as my advisor. I also wish to thank my committee members Professors Lang and Peng, for their helpful guidance on how to improve my work. Professor Lang took the time to explain answers to any questions I had over the years. I learned a lot from these discussions and I am grateful I had that opportunity to learn from him. Professor Peng made the collaboration happen between MIT and the National University of Singapore (NUS). It was one of the highlights of my PhD experience. He was always very welcoming to me whenever I visited NUS or the Masdar Institute in Abu Dhabi and I express my gratitude for this.

Part I of this thesis arose from a collaboration with Mohammad Qasim and Matthew Overlin. I offer my sincere gratitude to both of them for helping out with this - in particular, they both helped enormously in addressing reviewers' comments when we were trying to get that paper published.

Part II of this thesis stems from a collaboration between MIT and NUS. I wish to thank both Gurupraanesh Raman and Jerry Lu for the enormous amount of work put into this project. I wish to acknowledge Jerry for all of the hours he spent tuning hyperparameters and working on making our models better in general. I also want to thank Praanesh for developing this framework with me and for all the late nights, early mornings and brainstorming we did. I wish to also thank Krishan Kant who helped with the damping case study.

I express gratitude to my office-mates Mohammad Qasim, Sajjad Mohammadi

and Krishan Kant for making work such a fun place to be. I learned a lot from each of them, both technical and about life in general. I couldn't imagine doing research without having them all to discuss ideas with. I wish to thank the rest of Professor Kirtley's group and the students and staff at LEES in general, past and present. I am grateful to be in such a positive lab environment where there is a culture of helping each other out. There are too many names to mention here so at the risk of forgetting someone I express gratitude for them all. I am thankful for all of the staff at the EECS Headquarters. In particular, I wish to thank Janet Fisher, Alicia Duarte, Claire Benoit and Leslie Kolodziejski.

I am thankful for all of the teachers I had through the years. After 24 years in education, that number is probably fairly high. I acknowledge all of the staff I was fortunate to learn from at Walsh Island national school, Coláiste Íosagáin in Portarlington and at the National University of Ireland, Galway. In particular, I acknowledge my secondary school maths teacher Mr. Aughney, my thermodynamics lecturer Nathan Quinlan, as well as Rory Monaghan and Ger Hurley who both encouraged me to apply to MIT. I also acknowledge mentors who offered help and advice whenever I needed it: Frankie O'Sullivan, Ronán McGovern and Kevin O'Keeffe.

I would like to thank everyone involved in the MIT Rowing Club and the MIT Hyperloop team. A special thanks to my bandmates and great friends Gus Lonergan and Pavel Chvykov for filling my life with music. Each of these groups were a huge part of my experience and I have many memories as a result. I am grateful for all of the friends I made at MIT and in Boston in general. I would like to thank them all for making this feel like home. In particular I wish to thank the MIT Irish society and the general Irish community here in Boston for all of the laughs and good times. I would like to thank my roommates over the years for making my home a place I was happy to return to after a long day's work. Again, there are too many names to mention with each of these groups so I acknowledge all of them and I look forward to making new memories with them all in the future.

Finally, and most importantly, I wish to thank my family and extended family at home in Ireland and abroad. In particular, I wish to thank my parents Mary and

Michael and my siblings Evelyn, Tadhg, Matthew and Michael. They were always there to support me and growing up I felt confident I could become whatever I wanted thanks to them. I have a great family community and I am grateful and lucky to have them all. *Go raibh maith agaibh go léir.*

Maireann na daoine ar scáil a chéile

Contents

List of Figures

List of Tables

Chapter 1

Introduction

Electricity provides the foundation for many of today's technological advances. The desire for energy security, a reduction in carbon dioxide emissions and a diversification of resources are all motivations for changes in how electricity is generated and transmitted. Recent alternatives to traditional centralized power-plants include technologies that are decentralized and intermittent, such as solar photovoltaic and wind power. This trend poses considerable challenges in the hardware making up these systems, the software that control and monitor power networks and their mathematical modelling.

Traditional centralized power systems consist of sources in the form of coal, gas, nuclear and hydro power plants. The synchronous machine is at the heart of the mechanical to electrical energy conversion process, for each of these centralized power plants. As more renewables such as wind and solar penetrate the electricity grid, the percentage of non-inertial generation on the system increases. Many of these renewable technologies use DC to AC converters at their interface, meaning that the synchronous machine may not dominate power systems in the same way as it has in the past. Although the generation of electricity increasingly relies on a mix of technologies, these technologies use common mathematical tools (such as transformations) that were derived with respect to a specific application. For example the Park transformation was derived to help in the modelling of synchronous generators, yet this transform finds uses in numerous other fields including inverter control. The d and q

axes have physical meaning when referring to a synchronous machine, yet three-phase inverters often make use of the Park transformation. This motivates an alternative interpretation of reference-frames which is agnostic to a specific application. This is the first area of contributions in this thesis.

The second area of contributions focuses on the implications of decentralized power systems on the system operator. Decentralization can cause increased variability in the system, as the number of renewable energy sources connected to the grid increase. System operators must maintain system stability in spite of system changes such as faults, fluctuating supply and demand and alternate network topologies. In order to make dynamic decisions to maintain stability, the system operator first needs to have a better sense of the system health. This motivates a stability region generation tool that operators can use to view how stability regions are changing in real-time. This is the second area of contributions in this work.

1.1 Thesis Structure

This thesis outlines two solutions regarding the decentralization of power systems: Geometric Reference-Frame Theory and Stability Region Generation. As the technical details of these solutions are quite distinct, they are separated into Part I (geometric reference-frame theory) and Part II (stability region determination). Despite this distinct structure, Part I and Part II make up two solutions to a single application: decentralized generation in power systems.

The author directs the reader to the beginning chapter of each section for a literature review for each of the problems, as well as a list of contributions made using the proposed approaches.

Part I

A Geometric Interpretation of Reference-Frames

Chapter 2

Reference-Frame Theory

This chapter provides an overview of Part I of this thesis. The objective of this thesis is to address challenges associated with the decentralization of generation in power systems. Traditional centralised power systems have been dominated by the synchronous machine for the past 100 years. An increased proportion of renewables often leads to a higher proportion of inverters interfacing with the electricity network. This is because many renewable technologies such as solar photovoltaic and wind-farms require DC to AC converters at their interface. As the number of inverters increases, the synchronous machine may not dominate power system generation as it has done in the past. Transformations such as the Clarke transformation were derived with the intention to analyse specific problems such as unbalanced three-phase faults, yet somehow find uses in numerous other applications including three-phase inverter control. This motivates an alternative interpretation of reference-frames which is agnostic to a specific application. This problem is the focus of Part I of this thesis, which provides a solution in the form of a geometric interpretation of reference-frame theory [1].

2.1 Overview and Motivation

A reader familiar with the commonly used Clarke and Park transformations may wonder as to why one would want to investigate them further. One could argue

that the transformations already exist and therefore what benefit is there in additional research? The motivation to contribute to reference-frame theory stem from two main observations: (i) the Clarke and Park transformations were derived with respect to specific applications in mind, yet somehow both find uses in many applications beyond their original intention and (ii) signals with unbalance and harmonics have interesting properties when observed in the $dq0$ frame. Beyond this, the author believes there is value in a more general framework to understand these transformations, as this can allow one to gain a deeper understanding and intuition. One could also compare this to the analogy of music versus music theory. Music has existed since the early days of humankind - long before music theory was developed. Yet, the theoretical framework for music somehow makes it more rich and interesting for some people. Similarly, the Clarke and Park transformations already exist, but perhaps the geometric interpretation provided here adds depth to the field of reference-frame theory.

Transformations between abc and $dq0$ reference-frames were originally used to assist in electrical machine analysis and modelling [2]. Currently, $dq0$ based models are used in a wide variety of applications including: modelling and control of electric machines and drives [2, 3], multimachine modelling [4], multi-inverter modelling [5], microgrid simulation [6–8], phase-locked loops (PLLs) [9] and active power filters [10]. In many of these examples, the dq components no longer refer to the direct and quadrature axes of a machine. This motivates an alternative interpretation of reference-frames that is detached from any specific technology or application. This thesis provides one such alternative perspective which is referred to as the "geometric interpretation".

2.2 Previous Work

Considering the wealth of literature available on the subject of reference frames, it is essential that the contributions of this work are positioned in the context of previous work. To this end, the history of these transformations must first be studied,

taking care to cite the most notable references. Krause's arbitrary reference-frame and how this perspective relates to each transformation is reviewed. Following this, the geometric approach to deriving the Clarke and Park transformation matrices is presented. The contributions of this thesis are distinguished from previous work, and the advantages and disadvantages of the geometric approach are discussed.

2.2.1 Review of the Clarke and Park Transformations

Fig. 2-1 provides an overview of the transformations. The Clarke transformation converts three-phase abc quantities to $\alpha\beta 0$ (ie stationary $dq0$). The Park transformation converts abc quantities to $dq0$ and can be thought of as applying the Clarke transformation first, followed by the $\alpha\beta 0$ to $dq0$ transformation. Here the latter is simply referred to as the "$dq0$ transformation" for simplicity of subscript notation. Later it will be discussed how this corresponds to the "frame-to-frame-transformation" as described in [2].

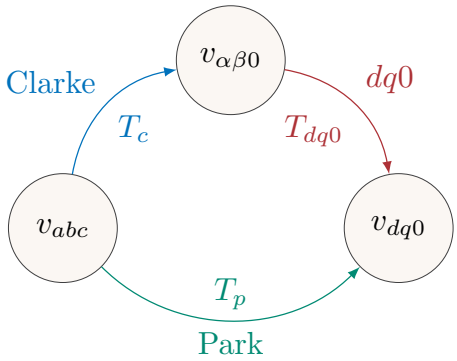

Figure 2-1: Relationships between the Park and Clarke transformations. Note that the term "$dq0$ transform" as defined in this thesis refers to a transformation from $\alpha\beta 0$ to $dq0$ and is therefore not equivalent to the Park transformation.

Fig. 2-2 shows the affect of applying the standard Clarke and Park transformations under three different conditions: (i) Balanced voltages result in equal magnitudes for v_α and v_β and constant values of v_d and v_q. (ii) Unbalanced voltages result in unequal magnitudes for v_α and v_β and time-varying v_d and v_q at the 2^{nd} harmonic. v_0 is a zero-sequence component at the fundamental and is always identical in both transformations.

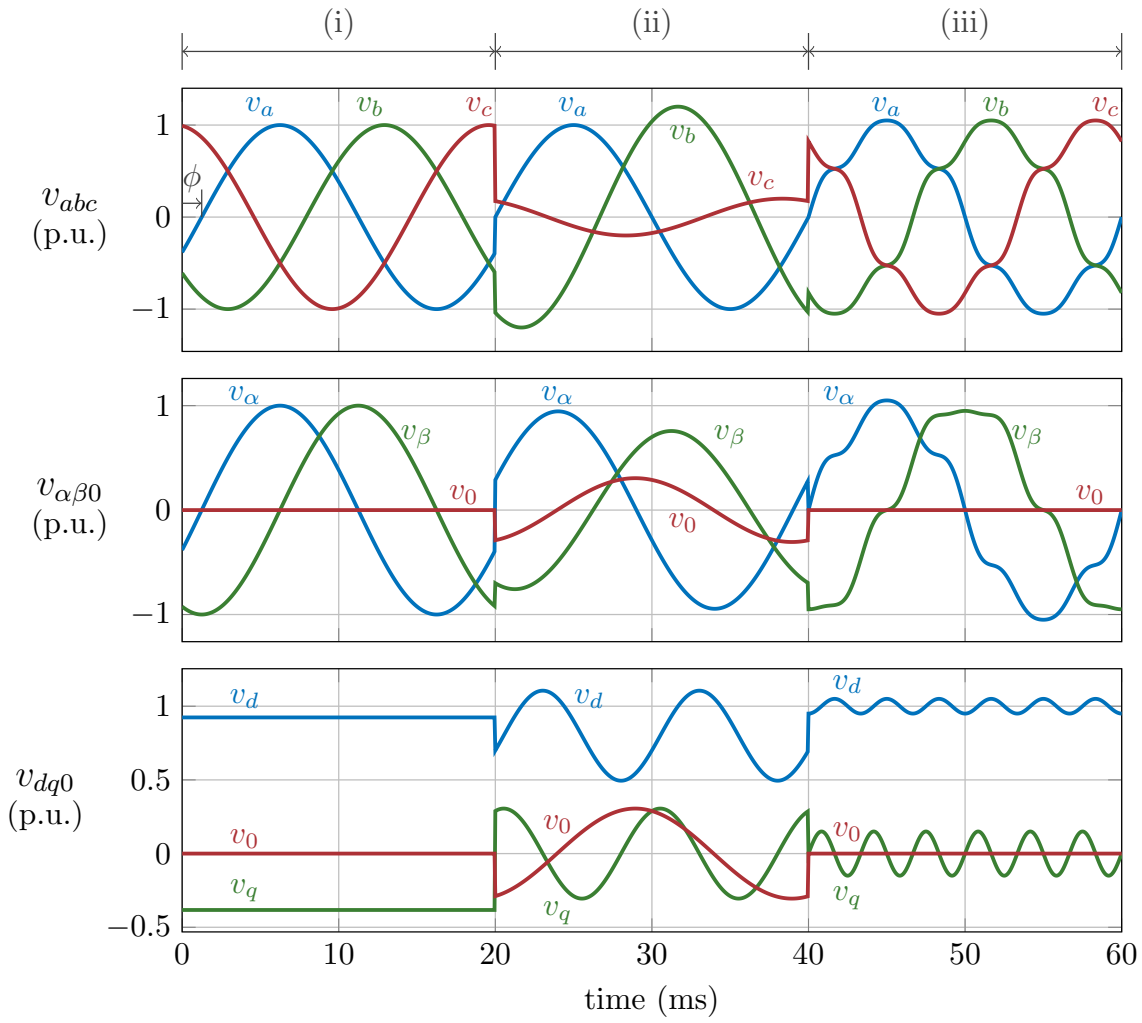

Figure 2-2: Clarke and Park transformations applied to three-phase 50 Hz voltages under three conditions: (i) balanced fundamental frequency with a phase shift (ii) unbalanced fundamental (iii) balanced with harmonics (1^{st}, 5^{th}, 7^{th}).

Condition (iii) in Fig. 2-2 illustrates the affect of harmonics. Each phase voltage includes fundamental, 5^{th} and 7^{th} harmonics, with balanced voltages at each harmonic. These particular harmonics appear as a 6^{th} harmonic in v_d and v_q. There is no zero-sequence component for these particular harmonics. The voltage v_α is equivalent to v_a; and v_β has a different harmonic profile to v_b due to a 180° phase-shift on its positive sequence components. In Section 3.3, each of the conditions (i), (ii) and (iii) in Fig. 2-2 are explained using the geometric interpretation.

History of the Clarke Transformation

In 1912, Stokvis introduced the concept of decomposing unbalanced three-phase signals into positive and negative sequence [11]. His example in [11, 12] describes a three-phase generator with a floating neutral node, and how unbalanced currents in such a system can be decomposed into "synchronous" and "inverse" currents (ie positive and negative sequence currents). Fortescue built on the work of Stokvis by introducing zero-sequence and generalising the decomposition for N phases in [13].

In the 1930s, Clarke made a series of modifications to symmetrical components [14, 15]. These modifications simplified the calculations for certain classes of unbalanced three-phase problems [15, 16]. The α, β and 0 components were one set of these innovations [15], and were particularly useful as they did not require the $\underline{a}$ operator ($1\angle\underline{120°}$) or complex numbers. Although Clarke's derivation in Fig. 2-3 requires both the $\underline{a}$ operator and a multiplication by j, the resulting transformation matrix does not contain any complex numbers, unlike the symmetrical components transformation.

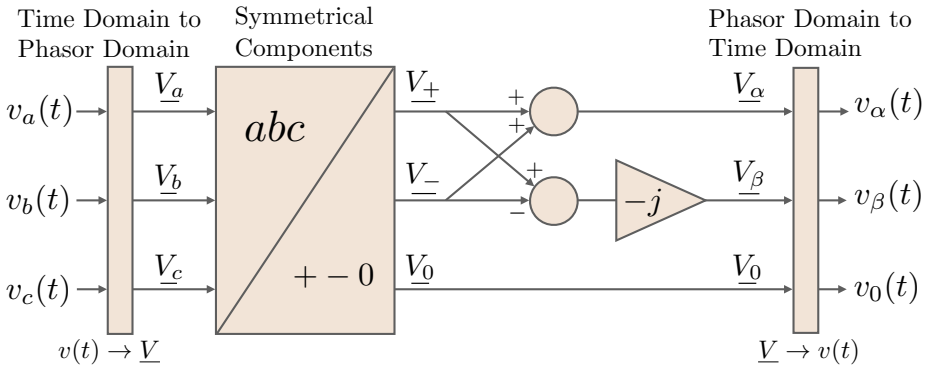

Figure 2-3: An illustration of the Clarke transformation as derived in [15].

Fig. 2-3 provides an illustration of the derivation developed by Clarke. The α component is defined as the sum of the positive and negative sequence voltage phasors, whereas the β component is the difference between positive and negative sequence phasors, times $-j$. Clarke's 0 component is equivalent to the zero sequence as defined by symmetrical components. For a comprehensive discussion of Clarke's derivation, the author refers the reader to [15].

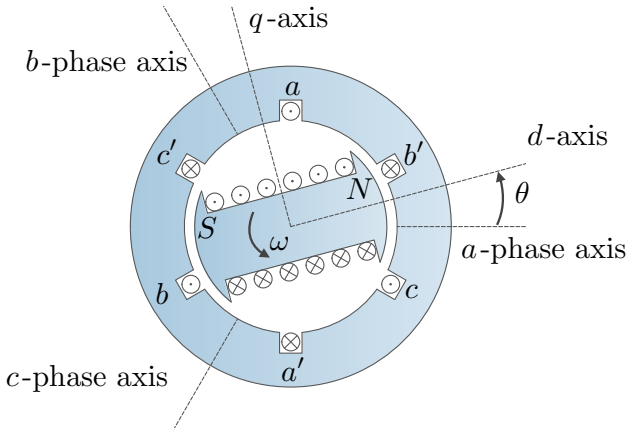

Figure 2-4: Cross-section of a synchronous machine

History of the Park Transformation

In 1899, Blondel developed the two-reactance method to study the behaviour of synchronous machines [17, 18]. This method resolves the armature fluxes in a salient machine along the two axes of symmetry: the direct and quadrature axes. Fig. 2-4 shows the physical definitions of the direct and quadrature axes.

During the 1920s, Park generalised Blondel's Two-Reaction Theory of Synchronous Machines [17–20]. This method resolves the armature fluxes in a salient machine along the two axes of symmetry: the direct and quadrature axes. Fig. 2-4 shows the physical definitions of the direct and quadrature axes. This thesis uses the convention that the d-axis points in the direction of the rotor flux. Park's derivation shown in Fig. 2-5 actually defines the inverse transformation: $dq0$ to abc. The steps are as follows: Firstly, assume that armature flux linkages can be resolved into two components: directly in phase with the rotor (λ_d) and in quadrature with the rotor (λ_q). Secondly, project the d and q-axes flux linkages onto the three coplanar abc magnetic axes. Finally, add a zero sequence component (λ_0) to each phase. The reader is referred to [19] for a more complete description of Park's derivation.

2.2.2 Review of the Arbitrary Reference-Frame

A "reference-frame" refers to a set of $dq0$ axes rotating at a particular speed ω (which may be zero). In the 1920s Park chose to rotate his $dq0$ axes as defined in [19] at

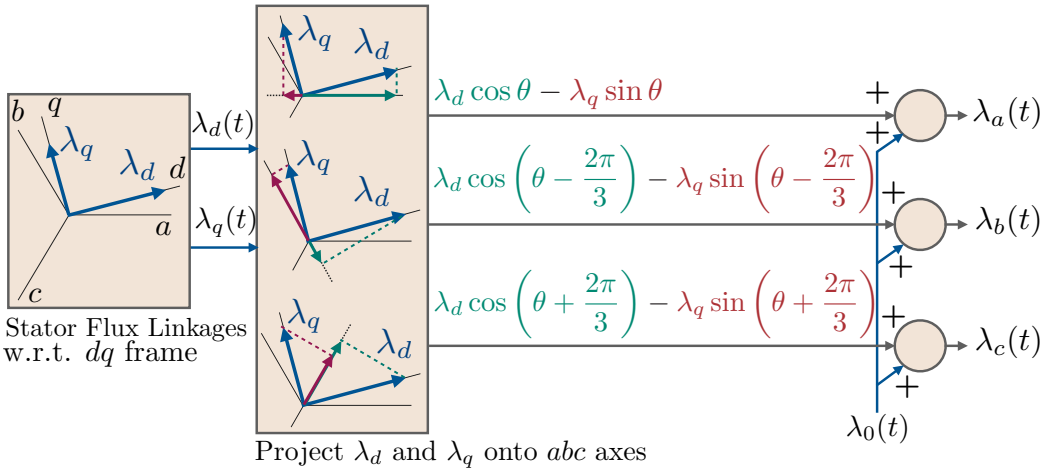

Figure 2-5: An illustration of the Park transformation as derived in [19]

the rotor speed of a synchronous machine ω_r (because that speed eliminates time-varying inductance in synchronous machine analysis). During the 1930s-1950s others [21–23] used alternative reference speeds for their $dq0$ axes, to assist in the analysis of induction machines. Eliminating time-varying inductance in addition to achieving a diagonalised inductance matrix were primary objectives [2].

In 1965, Krause described in [24] that all of the different reference-frames used in [15, 19, 21–23] are specific applications of the "arbitrary reference-frame". They all refer to $dq0$ axes that rotate at a specified ω. A list of commonly used reference-frame speeds are given below [2]:

- ω. The $dq0$ axes rotate at an *arbitrary* speed. [24].
- $\omega = \omega_r$. The $dq0$ axes rotate at the *rotor* speed [19].
- $\omega = \omega_e$. The $dq0$ axes rotate at the *synchronous* speed.
- $\omega = 0$. The $dq0$ axes are *stationary* (Clarke transformation).

All of the reference-frames listed can be described by Park's transformation matrix, except that each uses a different rotation speed ω for the $dq0$ axes. The reader is referred to [2] for an extensive discussion of the various reference-frames.

One of the goals of this work is to provide an alternative derivation of Park's transformation matrix, which describes all of the listed reference-frames (when the

appropriate ω is inserted into this matrix). Therefore, a general approach is taken here and an arbitrary reference speed ω is considered when referring to Park's transformation matrix. This matrix is still referred to as "Park's transformation", even though the reference speed is not limited to be that of the rotor ω_r. One is free to choose any reference speed they wish.

2.3 Contributions to Reference-Frame Theory

The contributions of this thesis in the area of reference-frame theory are summarised below. The remainder of this section elaborates on these points:

1. Previous approaches to deriving the matrices describing the Park and Clarke transformations are grouped into two approaches. This work presents a third approach to deriving the Clarke and Park transformation matrices: a geometric approach.

2. The "locus diagram" of a three-phase quantity is introduced along with demonstrations of how this locus changes in the presence of unbalance and harmonics.

The first contribution is to provide an alternative approach to derive the Park and Clarke transformations. Previous work on deriving these transformation matrices follows one of two approaches:

(i) The Clarke transformation matrix is derived from symmetrical components [15] as shown in Fig. 2-3. The Park transformation matrix can be subsequently derived using a rotation matrix such as Eq. (3.17).

(ii) The Park transformation matrix is derived trigonometrically by interpreting the transformation as a rotation in the plane of the cross-section of a machine. The *abc* axes are coplanar stationary axes that lie 120° apart and *dq* quantities can be projected onto the *abc* axes in a manner shown in Fig. 2-5. A third transformation variable is introduced to satisfy the change of variables. This is chosen to be the zero component, which is added separately. Many authors

trigonometrically project in the opposite manner: from *abc* to *dq* and are thus required to specify scaling factors k_d and k_q, normally equal to either 2/3 or $\sqrt{2/3}$: see [25]. These projections describe the approach taken by the majority of authors such as [2, 19, 21–28]. The Clarke transformation matrix can then be derived trivially by setting $\omega = 0$ in Park's transformation matrix. One should note that the coplanar *abc* axes are usually considered to have a physical meaning relating to the magnetic axes in the cross-section of a machine as in Fig. 2-4, but this physical interpretation of the *abc* axes is not necessary to derive the matrix [2].

This thesis section presents a third approach to deriving the Clarke and Park transformation matrices: a geometric interpretation. This geometric approach uses the Cartesian representation: three-phase quantities are represented by vectors in $\mathbb{R}^3$, where each orthogonal component of the vector corresponds to the instantaneous value of one of the three phases. The first appearance of the Cartesian representation applied to three-phase quantities was given by Lipo in [29]. Other work that uses this representation includes [30, 31]. More recently, Montanari and Gole use a three-dimensional perspective to introduce a new transformation termed the "*mno*-transform" [32]. The *mno*-transformation assists in the calculation of instantaneous real and reactive power for systems containing four-wire inverters. This enables the mitigation of power oscillations that normally occur when such systems are unbalanced [32]. Although others have utilised the Cartesian representation in [29–32], this work is unique as the representation is used to derive the matrices describing the Clarke and Park transformations.

The geometric approach is explained step-by-step in Section 3.1 and Section 3.2. A summary of the derivations provided by the geometric view is given by Fig. 2-6. Each transformation is interpreted as a combination of vector rotation and scaling in $\mathbb{R}^3$. The *abc* axes are orthogonal stationary axes that lie 90° apart and have basis vectors that span $\mathbb{R}^3$. The linearity property of matrix transformations is exploited, and each transformation matrix can be derived by observing how each transformation affects the orthonormal basis vectors of the vector space.

The geometric approach has many advantages when compared to the two traditional approaches listed previously. These include:

- When trigonometrically deriving the Park transformation such as in Fig. 2-5, zero-sequence components are treated separately in the derivation. The d and q components are found from a projection operation whereas the 0 components are added separately. The geometric approach finds all $dq0$ components in a unified manner via Eq. (2.5).

- The previous approaches interpret the Clarke transformation as either a manipulation of symmetrical components as in Fig. 2-3, or as a specialised case of the arbitrary reference-frame with stationary $dq0$ axes [2]. The geometric approach interprets the power-invariant Clarke transformation as a single rotation in $\mathbb{R}^3$, which some readers may find to be a simpler explanation (see Fig. 3-1). The standard (amplitude-invariant) Clarke transformation is shown in Fig. 3-3 to be a combination of rotation and scaling in $\mathbb{R}^3$.

- Similarly, previous approaches interpret the Park transformation as either a manipulation of symmetrical components [15] combined with a rotation matrix, or as a projection onto coplanar abc axes [19]. The geometric approach interprets the power-invariant Park transformation as two consecutive rotations in $\mathbb{R}^3$, which some readers may find to be more intuitive (see Fig. 2-6). The standard Park transformation is interpreted as first applying the standard Clarke transform (rotation and scaling) followed by a pure rotation in $\mathbb{R}^3$ given by Fig. 3-5.

- The orthogonality ($\boldsymbol{A}^{\intercal} = \boldsymbol{A}^{-1}$) of the power-invariant forms of both transformations can be easily seen from all three approaches via matrix manipulation. The geometric interpretation illustrates this orthogonal property: orthogonal transformations preserve vector length and can thus be visualised as pure rotations in $\mathbb{R}^3$ [33].

The disadvantages of the geometric interpretation, compared with the two traditional

approaches include:

- The geometric derivation is more involved. This can be seen by comparing Fig. 2-6 to the two traditional approaches illustrated by Fig. 2-3 and Fig. 2-5.
- The diagrams required to explain the geometric view are more complex to draw as they are three-dimensional.

The second contribution involves the "locus diagram" of a three-phase quantity and how this locus changes in the presence of unbalance and harmonics. This contribution consists of the following:

- In Section 2.5.1 it is shown that for balanced systems, the locus corresponds to a circle in $\mathbb{R}^3$. Eq. (2.13) is used to show that this circle has a radius of $V\sqrt{3/2}$ where V is the voltage magnitude on each phase.
- In Section 3.3 the locus diagram is extended to cases of harmonics and unbalance. Systems with purely positive and negative sequence will have a locus that lies within the $\alpha\beta$-plane. The locus of a zero-sequence component is a line segment perpendicular to the $\alpha\beta$-plane.
- It is shown that a single locus diagram can fully represent a three-phase quantity containing harmonics in Fig. 3-11. This is not possible using a single phasor diagram.

2.4 Review of Linear Transformations

Transformations are functions that operate on vectors. This section derives a basic method to finding a unique matrix $\boldsymbol{A}$ that fully describes a linear transformation $T\colon \mathbb{R}^n \to \mathbb{R}^m$.

Any vector $\vec{v} \in \mathbb{R}^n$ can be written as a linear combination of the standard basis unit vectors $\{\hat{\mathbf{e}}_1, \hat{\mathbf{e}}_2, \ldots, \hat{\mathbf{e}}_n\}$.

$$\vec{v} = v_1\hat{\mathbf{e}}_1 + v_2\hat{\mathbf{e}}_2 + \ldots + v_n\hat{\mathbf{e}}_n \tag{2.1}$$

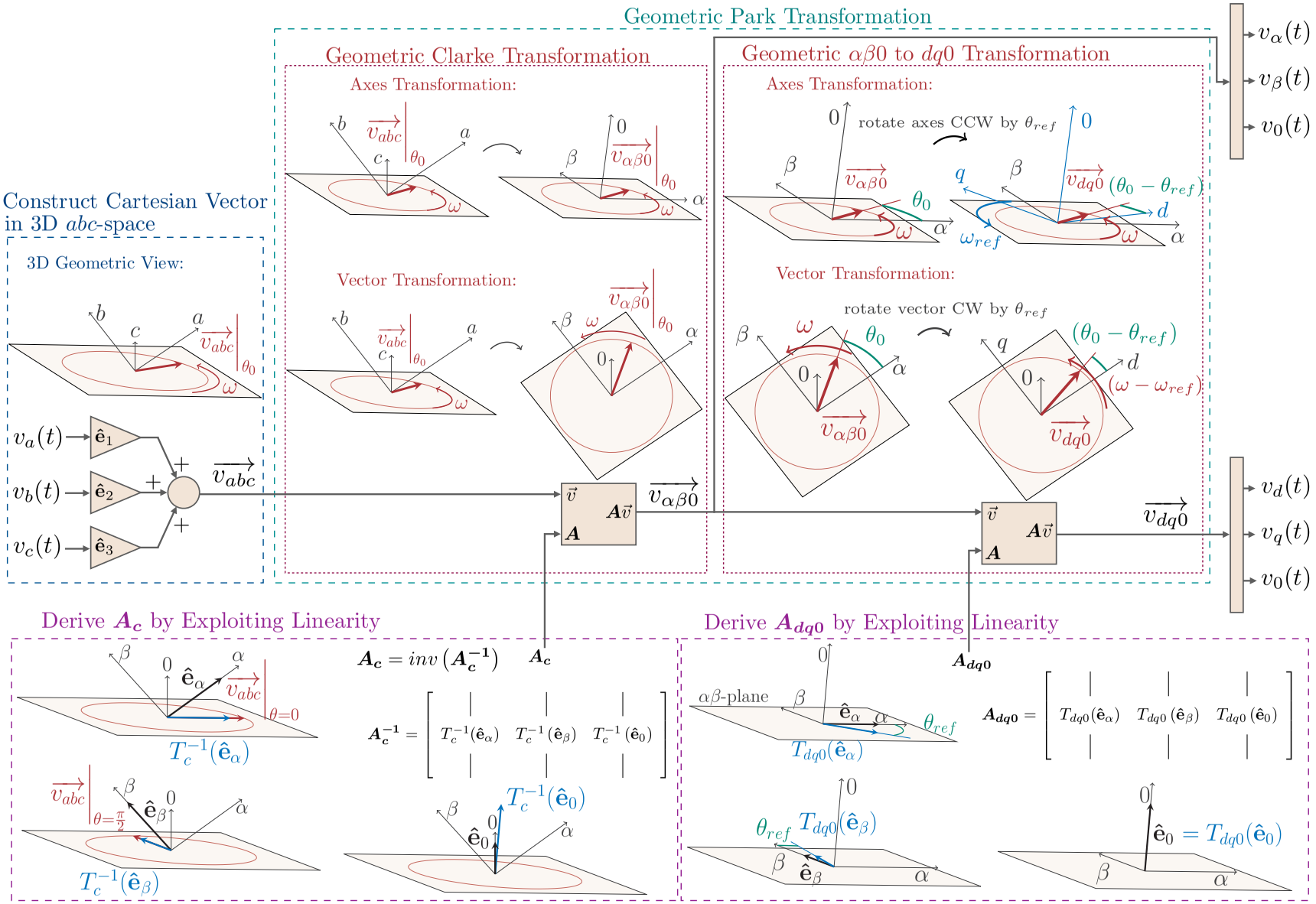

Figure 2-6: Geometric interpretation of the Clarke and Park transformations.

To find $T(\vec{v}) \in \mathbb{R}^m$ the linear transformation T is applied to both sides of equation 2.1:

$$T(\vec{v}) = T(v_1\hat{\mathbf{e}}_1 + v_2\hat{\mathbf{e}}_2 + \ldots + v_n\hat{\mathbf{e}}_n) \tag{2.2}$$

One can rewrite $T(\vec{v})$ by imposing the additivity and homogeneity constraints of linearity:

$$T(\vec{v}) = v_1T(\hat{\mathbf{e}}_1) + v_2T(\hat{\mathbf{e}}_2) + \ldots + v_nT(\hat{\mathbf{e}}_n) \tag{2.3}$$

$T(\vec{v})$ in equation 2.3 is now expressed in terms of transformed standard basis vectors scaled by the components of $\vec{v}$. Such a linear combination of column vectors can always be written as a matrix-vector product:

$$T(\vec{v}) = \begin{bmatrix} | & | & & | \\ T(\hat{\mathbf{e}}_1) & T(\hat{\mathbf{e}}_2) & \ldots & T(\hat{\mathbf{e}}_n) \\ | & | & & | \end{bmatrix} \begin{bmatrix} v_1 \\ v_2 \\ \vdots \\ v_n \end{bmatrix}$$

$$T(\vec{v}) = \boldsymbol{A}\vec{v} \tag{2.4}$$

Eq. (2.4) says that any linear transformation $T\colon \mathbb{R}^n \to \mathbb{R}^m$ can be expressed as a matrix-vector product $\boldsymbol{A}\vec{v}$.

$$\boldsymbol{A} = \begin{bmatrix} | & | & & | \\ T(\hat{\mathbf{e}}_1) & T(\hat{\mathbf{e}}_2) & \ldots & T(\hat{\mathbf{e}}_n) \\ | & | & & | \end{bmatrix} \tag{2.5}$$

Eq. (2.5) describes a technique to determine the $m \times n$ matrix $\boldsymbol{A}$, that corresponds to the linear transformation $T\colon \mathbb{R}^n \to \mathbb{R}^m$. One can construct $\boldsymbol{A}$ by applying the linear transformation to each of the basis vectors of $\mathbb{R}^n$. Eq. (2.5) is used in this thesis to geometrically derive the Park and Clarke transformation matrices $\boldsymbol{A}_P$ and $\boldsymbol{A}_C$.

2.5 Cartesian Representation of Three-Phase Voltages

Three-phase quantities such as voltages, currents and flux linkages are often expressed using phasor notation. This section introduces the Cartesian representation and compares it with phasor notation.

Phasor Representation

Eq. (2.6) is an example of a set of three-phase voltages with no harmonics. For now these voltages may or may not be balanced, where "balanced" would require $\phi_a = \phi_b = \phi_c = 0$ and $V_a = V_b = V_c$.

$$\begin{cases} v_a(t) = V_a \cos(\omega t + \phi_a) \\ v_b(t) = V_b \cos(\omega t - \frac{2\pi}{3} + \phi_b) \\ v_c(t) = V_c \cos(\omega t + \frac{2\pi}{3} + \phi_c) \end{cases} \tag{2.6}$$

Each of the three sinusoidal voltages in Eq. (2.6) can be represented by a unique phasor. Phasor notation is the use of a single complex known as a *phasor* to store the two parameters of magnitude V and phase ϕ. The magnitude of the phasor $\underline{V_i}$ represents the RMS value of $v_i(t)$ and the phase ϕ_i corresponds to the angle of the voltage $v_i(t)$.

Note that the expression for each sinusoidal voltage in Eq. (2.6) is actually defined by three parameters: voltage magnitude V_i, phase ϕ_i and frequency ω. A known frequency must be assumed, which is one limitation of the phasor representation. In addition, the phasor representation cannot be used to represent signals containing more than one frequency component, such as signals with harmonics.

Eq. (2.7) expresses the voltages in Eq. (2.6) as three phasors $\underline{V_a}, \underline{V_b}$ and $\underline{V_c}$. These three phasors can be drawn on a single complex plane in a phasor diagram. Fig. 2-7a

draws a balanced case.

$$\begin{cases} \underline{V_a} = \frac{1}{\sqrt{2}} V_a e^{j\phi_a} \\ \underline{V_b} = \frac{1}{\sqrt{2}} V_b e^{j\left(-\frac{2\pi}{3}+\phi_b\right)} \\ \underline{V_c} = \frac{1}{\sqrt{2}} V_c e^{j\left(\frac{2\pi}{3}+\phi_c\right)} \end{cases} \tag{2.7}$$

Each voltage phasor in Eq. (2.7) can be converted back to a function of time using Euler's relation as shown in Eq. (2.8).

$$v_i(t) = \sqrt{2}\ \Re\{\underline{V_i} e^{j\omega t}\} \tag{2.8}$$

Cartesian Representation

The notation $\overrightarrow{v_{abc}}$ is used to signify the Cartesian representation of a set of three-phase voltages. Previous work that uses the Cartesian representation applied to three phase quantities includes: [29–32]. $\overrightarrow{v_{abc}}$ is a single vector in $\mathbb{R}^3$ and has three components corresponding to three orthogonal *abc* axes:

$$\overrightarrow{v_{abc}} = v_a \hat{\mathbf{e}}_a + v_b \hat{\mathbf{e}}_b + v_c \hat{\mathbf{e}}_c \tag{2.9}$$

The components of Eq. (2.9) vary with time. Thus $\overrightarrow{v_{abc}}$ is a vector that moves in $\mathbb{R}^3$ over time as seen in Eq. (2.10):

$$\overrightarrow{v_{abc}}(t) = \begin{bmatrix} v_a(t) \\ v_b(t) \\ v_c(t) \end{bmatrix} = \begin{bmatrix} V_a \cos(\omega t + \phi_a) \\ V_b \cos(\omega t - \frac{2\pi}{3} + \phi_b) \\ V_c \cos(\omega t + \frac{2\pi}{3} + \phi_c) \end{bmatrix} \tag{2.10}$$

Fig. 2-7b plots $\overrightarrow{v_{abc}}(t)$ at a particular instance in time t_1. It will be seen later that the *locus* traced out by $\overrightarrow{v_{abc}}(t)$ over one period is of particular interest.

Fig. 2-7 compares the phasor and Cartesian representations for a three-phase system.

- Phasor Representation:

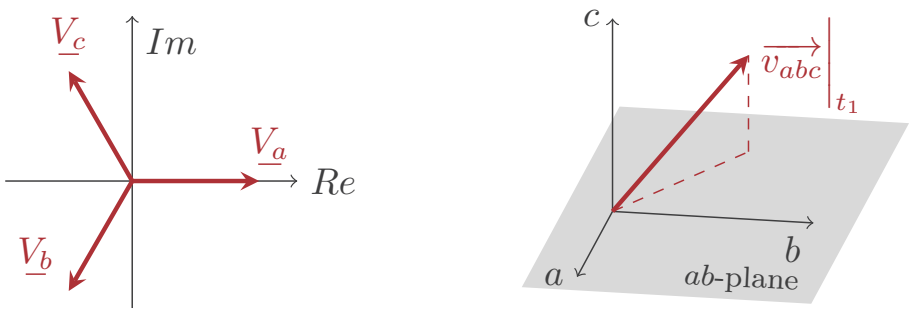

Figure 2-7: Three-phase voltage representations: (a) Phasor representation (b) Cartesian representation at time t_1.

  - $\mathbb{C}$ vector space with two axes Re and Im.
  - Three complex numbers (phasors) $\underline{V_a}, \underline{V_b}$ and $\underline{V_c}$ that do not vary with time.

- Cartesian Representation:
  - $\mathbb{R}^3$ vector space with three orthogonal axes a, b, c.
  - Single vector $\overrightarrow{v_{abc}}$ that moves with time.

2.5.1 The Locus of Balanced Three-Phase Voltages

The locus diagram is a complete graphical representation of a three-phase quantity. Whereas the phasor diagram of Fig. 2-7a cannot represent signals with more than one frequency component; the locus diagram can represent both harmonics and unbalance at each harmonic (See Section 3.3 for locus diagrams with harmonics and unbalance).

Fig. 2-8 is an example of a locus diagram. The voltages are defined by Eq. (2.10) for the balanced case, with peak magnitudes $V_a = V_b = V_c = V$ and $\phi_a = \phi_b = \phi_c$. The vector $\overrightarrow{v_{abc}}$ moves in $\mathbb{R}^3$ with time. This can be seen by examining how the orthogonal components of $\overrightarrow{v_{abc}}$ in Eq. (2.10) vary with time.

The locus is defined as the path in $\mathbb{R}^3$ that $\overrightarrow{v_{abc}}$ traverses over one cycle of the lowest frequency component. Fig. 2-8 shows that the locus of $\overrightarrow{v_{abc}}$ traces out a circle in $\mathbb{R}^3$ for a balanced set of three-phase voltages that contain no harmonics. $\overrightarrow{v_{abc}}$ rotates at a frequency of ω about this circle.

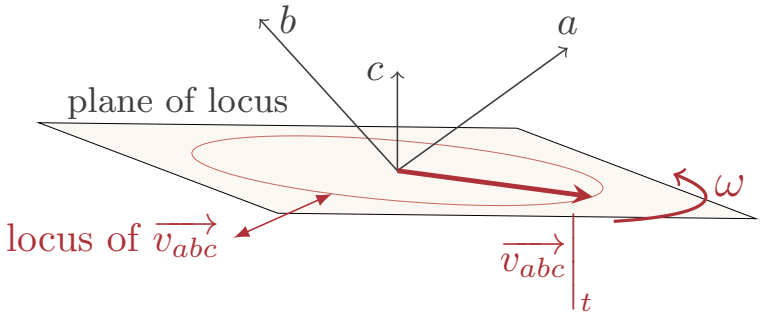

Figure 2-8: Locus diagram of balanced three-phase voltages.

The circular nature of the locus of balanced voltages may not be obvious at first, so this will be shown algebraically. If the length of the vector $\overrightarrow{v_{abc}}$ is constant for all of time, then the locus must trace out a circle. The euclidean distance in $\mathbb{R}^3$ is given by:

$$\|\overrightarrow{v_{abc}}(t)\| = \sqrt{v_a(t)^2 + v_b(t)^2 + v_c(t)^2} \tag{2.11}$$

Assuming balanced voltages with each phase having a peak magnitude of V, and each with a phase angle $\phi = 0$, one can rewrite Eq. (2.11) using Eq. (2.10) to give:

$$\|\overrightarrow{v_{abc}}(t)\| = V\left[\cos^2(\omega t) + \cos^2\left(\omega t - \frac{2\pi}{3}\right) + \cos^2\left(\omega t + \frac{2\pi}{3}\right)\right]^{1/2} \tag{2.12}$$

Eq. (2.12) can be rewritten using trigonometric identities to give:

$$\|\overrightarrow{v_{abc}}(t)\| = V\sqrt{\frac{3}{2}\sin^2(\omega t) + \frac{3}{2}\cos^2(\omega t)}$$

$$\|\overrightarrow{v_{abc}}(t)\| = V\sqrt{\frac{3}{2}} \quad \forall\ t \tag{2.13}$$

Eq. (2.13) shows that the locus of $\overrightarrow{v_{abc}}$ is a circle in $\mathbb{R}^3$ for a balanced set of three-phase voltages, as the vector length is constant. This circle is shown in Fig. 2-8 and has a radius of $V\sqrt{3/2}$ where V is the voltage magnitude on each phase.

This exercise of finding the length of $\overrightarrow{v_{abc}}$ also illustrates another important concept: the length of $\overrightarrow{v_{abc}}$ is not equivalent to the peak phase voltage, even when the

voltages are balanced. It is scaled by $\sqrt{3/2}$. This geometric analysis explains why the power-invariant Clarke and Park transformations have such scaling terms, as will be discussed in sections 3.1 and 3.2.

Chapter 3

Geometric Interpretations: dq0, Park, Clarke & Power Quality

3.1 Geometric Derivation of the Clarke Transformation

There are two versions of the Clarke transformation: the standard (amplitude-invariant) transformation and the power-invariant transformation. The derivation introduced by Clarke as shown in Fig. 2-3 is the amplitude-invariant form, which is the most commonly used version. It is convenient because the magnitude of v_α is the same as the magnitude of v_a when the voltages are balanced. Previous approaches to deriving the Clarke transformation either rely on a manipulation of symmetrical components [15], or use the arbitrary reference-frame with stationary axes [2]. In this section, the geometric approach is used to derive both the standard and power-invariant Clarke transformations. The power-invariant version is derived first, as it is geometrically simpler.

3.1.1 Power-Invariant Clarke Transformation Derivation

The power-invariant Clarke transformation is a pure rotation, such that the locus of a balanced three-phase quantity lies in the ab-plane (this ab-plane is referred to as

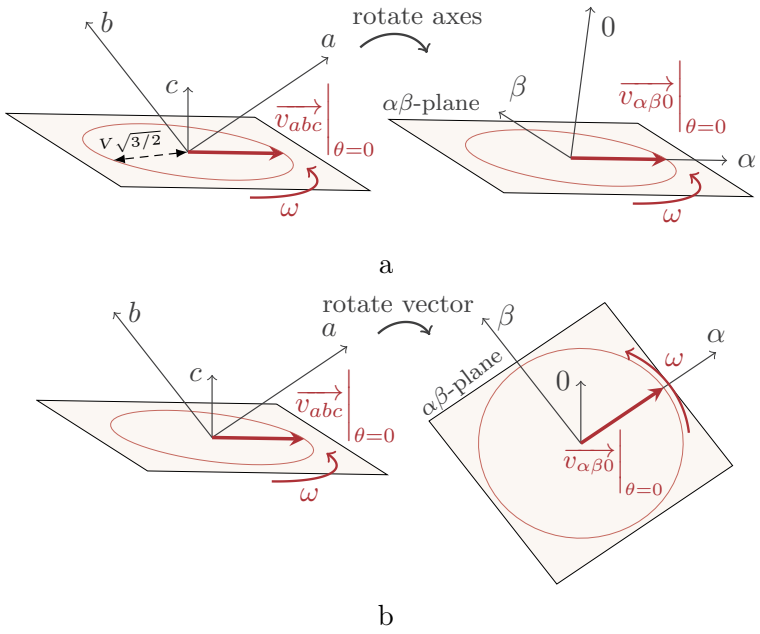

Figure 3-1: The power invariant Clarke transformation: (a) Axes transformation perspective: rotate the abc-axes such that the a-axis lines up with the vector v_{abc} at $\theta = 0$, and the b-axis also lies in the rotated ab-plane ($\alpha\beta$-plane). The rotated ab-axes become the $\alpha\beta$-axes respectively. The rotated c-axis becomes the 0-axis. (b) Vector transformation perspective: rotate the voltage vector v_{abc} such that its locus lies in the ab-plane.

the $\alpha\beta$-plane after the transformation is performed). Fig. 3-1 illustrates the locus diagrams for the geometric power-invariant Clarke transformation.

All transformations can be visualised as either a coordinate (axes) transformation or as a vector transformation. Fig. 3-1a is the axes transformation where the vector is fixed and the abc axes are rotated such that the locus of a balanced system lies in the rotated ab-plane (ie the $\alpha\beta$-plane). Fig. 3-1b is the vector transformation, where the axes are fixed and the vector rotates such that its locus lies in the ab-plane.

Note that there are infinite transformations that can achieve a locus that lies in the ab-plane, but only one of these anchor the α-axis so that it is in line with the balanced Cartesian voltage when the phase angle is zero ($\theta = \omega t + \phi = 0$), as seen in Fig. 3-1 . It will be shown later that this family of infinite transformations is given by Park's matrix where substituting a value of theta anchors the α-axis at a different location in the plane.

Using the constraints of bringing the locus into the ab-plane and anchoring the α-

axis appropriately one can determine the matrix associated with the power-invariant Clarke transformation. Eq. (2.5) (derived in Section 2.4) describes steps to find a matrix (e.g. $\boldsymbol{A_c}$) that represents a linear transformation (T_c). These steps require one to know how each orthonormal basis vector of a given space is affected by a transformation.

The inverse Clarke transformation T_c^{-1} is more convenient to derive geometrically than T_c. One can visualise how T_c^{-1} transforms vectors by reading Fig. 3-1 from right to left. The inverse transformation rotates the unit vectors $\hat{\mathbf{e}}_\alpha$ and $\hat{\mathbf{e}}_\beta$ such that they lie in the plane of $\overrightarrow{v_{abc}}$. Thus, these transformed unit vectors $T_c^{-1}(\hat{\mathbf{e}}_\alpha), T_c^{-1}(\hat{\mathbf{e}}_\beta)$ have a direction given by $\overrightarrow{v_{abc}}$ at angles of $\theta = 0$ and $\theta = \pi/2$ respectively. Whereas T_c rotates the abc unit vectors $\hat{\mathbf{e}}_a, \hat{\mathbf{e}}_b, \hat{\mathbf{e}}_c$ to a location that is inconvenient to determine.

$$\overrightarrow{v_{abc}} = T_c^{-1}\left(\overrightarrow{v_{\alpha\beta 0}}\right) = \boldsymbol{A_c^{-1}}\overrightarrow{v_{\alpha\beta 0}} \tag{3.1}$$

The matrix $\boldsymbol{A_c^{-1}}$ in Eq. (3.1) can be rewritten using Eq. (2.5):

$$\boldsymbol{A_c^{-1}} = \begin{bmatrix} | & | & | \\ T_c^{-1}(\hat{\mathbf{e}}_\alpha) & T_c^{-1}(\hat{\mathbf{e}}_\beta) & T_c^{-1}(\hat{\mathbf{e}}_0) \\ | & | & | \end{bmatrix} \tag{3.2}$$

These three steps of Eq. (3.2) are shown graphically in Fig. 3-2. Each step involves a rotation of a unit vector. The inverse power-invariant Clarke transformation T_c^{-1} is applied to each of the three $\alpha\beta 0$ unit vectors $\{\hat{\mathbf{e}}_\alpha, \hat{\mathbf{e}}_\beta, \hat{\mathbf{e}}_0\}$. Fig. 3-2a shows how $\hat{\mathbf{e}}_\alpha$ is transformed under the inverse power-invariant Clarke transformation. Its transformed direction is given by the Cartesian voltage when the angle is zero:

$$T_c^{-1}(\hat{\mathbf{e}}_\alpha) = \frac{\overrightarrow{v_{abc}}\Big|_{\theta=0}}{\|\overrightarrow{v_{abc}}\|} \tag{3.3}$$

It was shown in Section 2.5.1 that balanced three-phase systems have circular loci

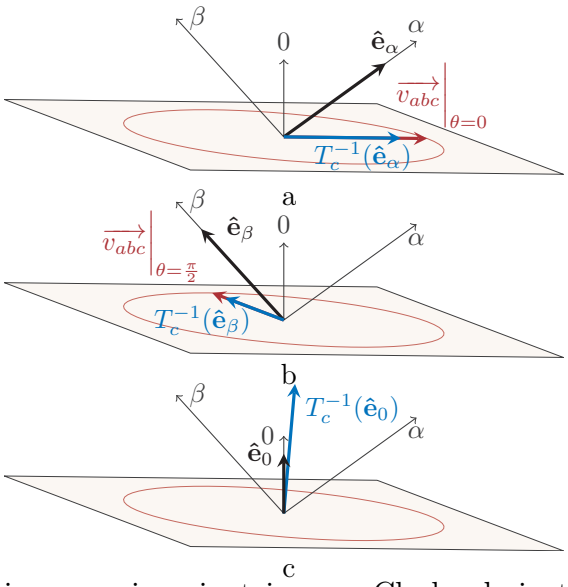

Figure 3-2: Geometric power-invariant inverse Clarke derivation: (a) rotate $\hat{\mathbf{e}}_\alpha$ to align with the vector v_{abc} at $\theta = 0$ (b) rotate $\hat{\mathbf{e}}_\beta$ to align with the vector v_{abc} at $\theta = \pi/2$ (c) rotate $\hat{\mathbf{e}}_0$ perpendicular to the plane. Note: This figure uses the vector transformation perspective shown in Fig. 3-1b. This perspective highlights how the unit vectors rotate, which allows us to evaluate Eq. (3.2)

with a radius given by Eq. (2.13). Substituting Eq. (2.13) into Eq. (3.3) gives:

$$T_c^{-1}(\hat{\mathbf{e}}_\alpha) = \frac{1}{V}\sqrt{\frac{2}{3}}\,\overrightarrow{v_{abc}}\Big|_{\theta=0} = \sqrt{\frac{2}{3}}\begin{bmatrix}\cos\theta\\ \cos\left(\theta-\frac{2\pi}{3}\right)\\ \cos\left(\theta+\frac{2\pi}{3}\right)\end{bmatrix}\Bigg|_{\theta=0} \tag{3.4}$$

$\overrightarrow{v_{abc}}$ is evaluated when the angle is zero:

$$T_c^{-1}(\hat{\mathbf{e}}_\alpha) = \sqrt{\frac{2}{3}}\begin{bmatrix}1 & -\frac{1}{2} & -\frac{1}{2}\end{bmatrix}^\intercal \tag{3.5}$$

Fig. 3-2b illustrates how the the unit vector $\hat{\mathbf{e}}_\beta$ is rotated to align with the Cartesian voltage when the angle is $\pi/2$.

$$T_c^{-1}(\hat{\mathbf{e}}_\beta) = \frac{\overrightarrow{v_{abc}}\Big|_{\theta=\frac{\pi}{2}}}{\|\overrightarrow{v_{abc}}\|}$$

$$T_c^{-1}(\hat{\mathbf{e}}_\beta) = \frac{1}{V}\sqrt{\frac{2}{3}}\,\overrightarrow{v_{abc}}\Big|_{\theta=\frac{\pi}{2}} = \sqrt{\frac{2}{3}}\begin{bmatrix} 0 & \frac{\sqrt{3}}{2} & -\frac{\sqrt{3}}{2}\end{bmatrix}^\intercal \tag{3.6}$$

In Fig. 3-2c it was seen how $\hat{\mathbf{e}}_0$ is rotated such that it is perpendicular to the plane of a balanced locus. Mathematically, this can be thought of as pointing in the direction of the cross product of $\hat{\mathbf{e}}_\alpha$ and $\hat{\mathbf{e}}_\beta$, as given by the right-hand rule:

$$T_c^{-1}(\hat{\mathbf{e}}_0) = \frac{\overrightarrow{v_{abc}}\Big|_{\theta=0} \times \overrightarrow{v_{abc}}\Big|_{\theta=\frac{\pi}{2}}}{\|\overrightarrow{v_{abc}}\Big|_{\theta=0} \times \overrightarrow{v_{abc}}\Big|_{\theta=\frac{\pi}{2}}\|}$$

$$T_c^{-1}(\hat{\mathbf{e}}_0) = \sqrt{\frac{2}{3}}\begin{bmatrix} \frac{1}{\sqrt{2}} & \frac{1}{\sqrt{2}} & \frac{1}{\sqrt{2}}\end{bmatrix}^\intercal \tag{3.7}$$

The three steps given by Eq. (3.5), Eq. (3.6) and Eq. (3.7) are combined with Eq. (3.2) to find $\boldsymbol{A_c^{-1}}$.

$$\boldsymbol{A_c^{-1}} = \sqrt{\frac{2}{3}}\begin{bmatrix} 1 & 0 & \frac{1}{\sqrt{2}} \\ -\frac{1}{2} & \frac{\sqrt{3}}{2} & \frac{1}{\sqrt{2}} \\ -\frac{1}{2} & -\frac{\sqrt{3}}{2} & \frac{1}{\sqrt{2}}\end{bmatrix} \tag{3.8}$$

The matrix $\boldsymbol{A_c^{-1}}$ is an orthogonal matrix because it is associated with a pure rotation. This means its transpose is equal to its inverse, $\boldsymbol{A_c} = \left(\boldsymbol{A_c^{-1}}\right)^\intercal$.

3.1.2 Standard Clarke Transformation Derivation

The standard (amplitude-invariant) Clarke transformation was originally derived by Clarke in a manner shown in Fig. 2-3. This section geometrically derives the amplitude-invariant Clarke transformation which has become the standard version.

The standard Clarke transformation is a rotation and scaling, such that the locus of a balanced three-phase quantity lies in the *ab*-plane with a radius equal to the phase magnitude. It can be thought of as first applying the pure rotation described by the power-invariant Clarke transformation followed by a scaling operation. Eq. (2.13)

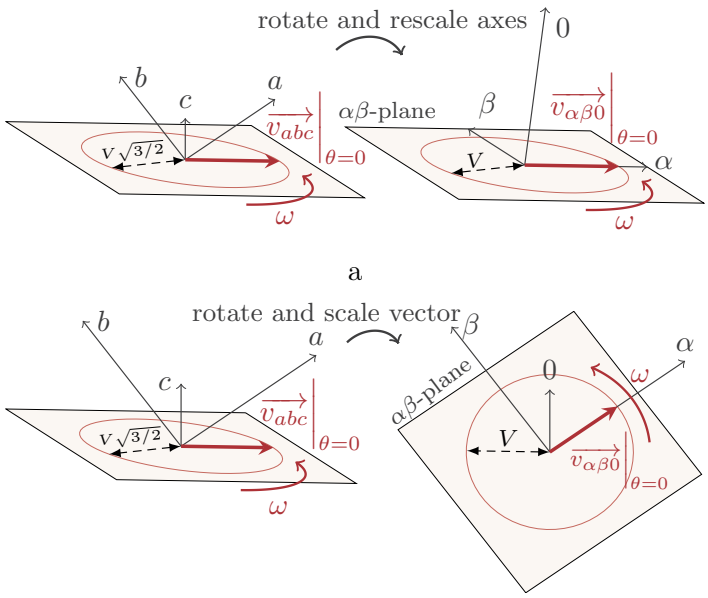

Figure 3-3: The standard (amplitude-invariant) Clarke transformation:(a) Axes transformation perspective: rotate the abc-axes such that the a-axis lines up with the vector v_{abc} at $\theta = 0$, and the b-axis also lies in the plane. Stretch the rotated ab-axes by $\sqrt{3/2}$ such that the circle traced by $v_{\alpha\beta 0}$ has a radius of V, when referenced to the $\alpha\beta$-axes. The rotated and stretched ab-axes become the $\alpha\beta$-axes respectively. The rotated c-axis becomes the 0-axis, and is stretched by $\sqrt{3}$ in order to agree with the definition of zero-sequence. (b) Vector transformation perspective: rotate the vector v_{abc} such that it lies in the ab-plane. Scale the rotated v_{abc} by $\sqrt{2/3}$ such that it has a length of V when referenced to the $\alpha\beta$-plane. The 0-component of the vector $v_{\alpha\beta 0}$ is scaled by $1/\sqrt{3}$ in order to agree with the definition of zero-sequence.

shows that the locus of a balanced three-phase voltage is a circle of radius $V\sqrt{3/2}$. The standard Clarke transformation scales this locus, such that the circle has a radius of V.

Fig. 3-3 illustrates the locus diagrams for the geometric amplitude-invariant Clarke transformation. Fig. 3-3a is the axes transformation where the vector is fixed and the abc axes are rotated such that the locus of a balanced system lies in the $\alpha\beta$-plane. The α and β axes are stretched by $\sqrt{3/2}$ such that the locus traced by a balanced voltage has a radius equal to V, the peak magnitude of the phase voltage. The 0-axis is stretched by $\sqrt{3}$ making this equivalent to the symmetrical components definition of zero-sequence. Whatever voltage exists on the 0-axis will appear with the same magnitude on the a, b and c axes.

Fig. 3-3b is the vector transformation, where the axes are fixed and the vector rotates such that its locus lies in the ab-plane. The vector's α and β components are scaled by $\sqrt{2/3}$, meaning the locus of a balanced Cartesian vector will appear as a circle with a radius of V when referenced to the $\alpha\beta 0$ axes. The 0-axis is scaled by $1/\sqrt{3}$ to match the symmetrical components definition of zero-sequence.

Just as with the power-invariant transformation, there are infinite transformations that can achieve a locus that lies in the ab-plane with the scaling described as above. However, only one of these ensure that the α-axis is in line with the balanced Cartesian voltage when the phase angle is zero ($\theta = \omega t + \phi = 0$).

The same procedure is followed as the power-invariant derivation. Once again, the matrix $\boldsymbol{A_c^{-1}}$ associated with the inverse transformation T_c^{-1} is found using Eq. (3.2). Please refer to Section 3.1.1 for a discussion on why the inverse Clarke transformation is derived.

The three steps described by Eq. (3.2) are shown graphically in Fig. 3-4. They involve transforming each of the three unit vectors under T_c^{-1}. Fig. 3-4a shows how $\hat{\mathbf{e}}_\alpha$ is transformed under the inverse standard Clarke transformation. $\hat{\mathbf{e}}_\alpha$ is rotated and stretched by $\sqrt{3/2}$, making it equivalent to the per-unit Cartesian voltage when the angle is zero.

$$T_c^{-1}(\hat{\mathbf{e}}_\alpha) = \overrightarrow{v_{abc}}\Big|_{\substack{V=1\\ \theta=0}} = \begin{bmatrix} V\cos\theta \\ V\cos\left(\theta - \frac{2\pi}{3}\right) \\ V\cos\left(\theta + \frac{2\pi}{3}\right) \end{bmatrix}\Bigg|_{\substack{V=1\\ \theta=0}}$$

$$T_c^{-1}(\hat{\mathbf{e}}_\alpha) = \begin{bmatrix} 1 & -\frac{1}{2} & -\frac{1}{2} \end{bmatrix}^\intercal \tag{3.9}$$

Similarly, Fig. 3-4b shows that $\hat{\mathbf{e}}_\beta$ is rotated and stretched by $\sqrt{3/2}$, making it equivalent to the per-unit Cartesian voltage when the angle is $\pi/2$.

$$T_c^{-1}(\hat{\mathbf{e}}_\beta) = \overrightarrow{v_{abc}}\Big|_{\substack{V=1\\ \theta=\frac{\pi}{2}}} = \begin{bmatrix} 0 & \frac{\sqrt{3}}{2} & -\frac{\sqrt{3}}{2} \end{bmatrix}^\intercal \tag{3.10}$$

Fig. 3-4c explains how $\hat{\mathbf{e}}_0$ is transformed. It points perpendicular to the plane in which the locus of $\overrightarrow{v_{abc}}$ lies, and is scaled by $\sqrt{3}$. The scaling is necessary so that the 0-component agrees with the 0-sequence as defined by symmetrical components.

$$T_c^{-1}(\hat{\mathbf{e}}_0) = \sqrt{3}\,\frac{\overrightarrow{v_{abc}}\Big|_{\theta=0} \times \overrightarrow{v_{abc}}\Big|_{\theta=\frac{\pi}{2}}}{\|\overrightarrow{v_{abc}}\Big|_{\theta=0} \times \overrightarrow{v_{abc}}\Big|_{\theta=\frac{\pi}{2}}\|} = \begin{bmatrix} 1 \\ 1 \\ 1 \end{bmatrix} \tag{3.11}$$

The three transformed unit vectors given by Eq. (3.9), Eq. (3.10) and Eq. (3.11) are combined with Eq. (3.2) to find $\boldsymbol{A_c^{-1}}$.

$$\boldsymbol{A_c^{-1}} = \begin{bmatrix} 1 & 0 & 1 \\ -\frac{1}{2} & \frac{\sqrt{3}}{2} & 1 \\ -\frac{1}{2} & -\frac{\sqrt{3}}{2} & 1 \end{bmatrix} \tag{3.12}$$

One can find $\boldsymbol{A_c}$ by taking the inverse of the matrix $\boldsymbol{A_c^{-1}}$.

3.2 Geometric Derivation of the Park Transformation

There are two versions of the Park transformation: the standard (amplitude-invariant) transformation and the power-invariant transformation. The derivation introduced by Park in Fig. 2-5 is the amplitude-invariant form, which is the most commonly used version. It is convenient because the magnitude of v_d is the same as the magnitude of v_a if two conditions are met: the voltages are balanced and the reference signal is in phase with phase a.

Previous approaches to deriving the Park transformation either use: trigonometric projection with coplanar abc axes [19] or modifying symmetrical components to obtain Clarke's matrix [15] and applying a rotation matrix. This section derives the Park transformation matrix using the geometric approach. The relationship between

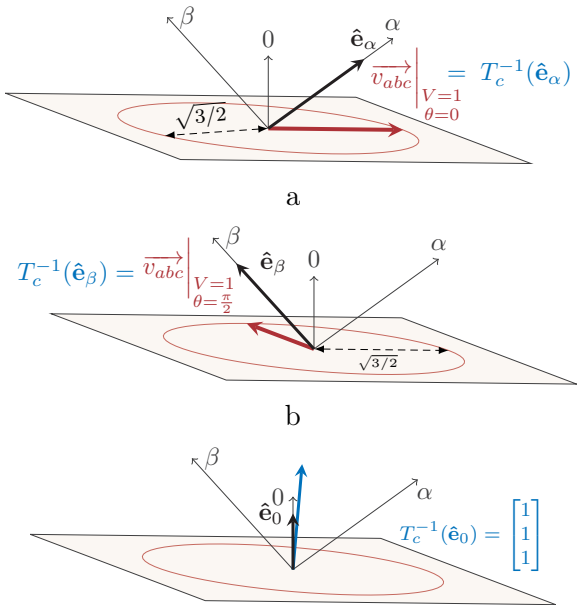

Figure 3-4: Geometric standard (amplitude-invariant) inverse Clarke derivation: (a) rotate $\hat{\mathbf{e}}_\alpha$ to align with the vector v_{abc} at $\theta = 0$ and stretch by $\sqrt{3/2}$ (b) rotate $\hat{\mathbf{e}}_\beta$ to align with the vector v_{abc} at $\theta = \frac{\pi}{2}$ and stretch by $\sqrt{3/2}$ (c) rotate $\hat{\mathbf{e}}_0$ perpendicular to the plane and stretch by $\sqrt{3}$. Note: This figure uses the vector transformation perspective shown in Fig. 3-3b. This perspective highlights how the unit vectors stretch and rotate, which allows us to evaluate Eq. (3.2)

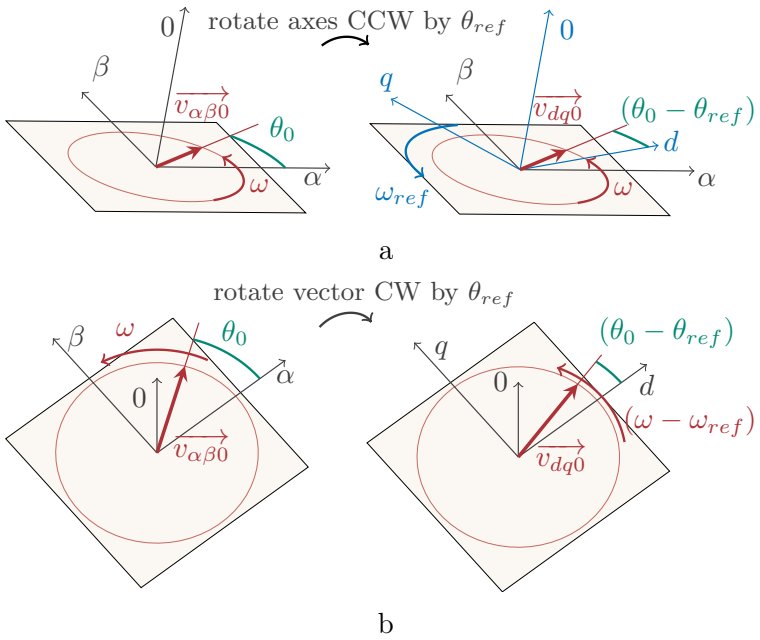

Figure 3-5: The $\alpha\beta 0$ to $dq0$ transformation: (a) Axes transformation perspective: rotate axes CCW about 0-axis by θ_{ref}. (b) Vector transformation perspective: rotate vector CW about 0-axis by θ_{ref}.

the Park and Clarke transformations as shown in Fig. 2-1 is utilised. The Park transformation can be decomposed into two consecutive transformations: the Clarke transformation followed by the $\alpha\beta 0$ to $dq0$ transformation. Section 3.1 details the geometric derivation of the Clarke transformation. This section completes the Park transformation matrix derivation by first deriving the $\alpha\beta 0$ to $dq0$ transformation. Then the Park transformation matrix is obtained by simple matrix multiplication. The overall geometric interpretation of the Park transformation is summarised in Fig. 2-6.

3.2.1 Transformation between Reference-Frames: $\alpha\beta 0$ to $dq0$ Transformation Derivation

The "transformation between reference-frames" or simply "frame-to-frame transformation" in [2] is used in multimachine [4] and multi-inverter modelling [5]. Each device is modelled in its own $dq0$ reference-frame, and each $dq0$ frame may have a different angle θ with respect to a common reference-frame. All devices can be translated to the common reference-frame using the transformation between two rotating $dq0$ frames [5]. The matrix describing this transformation has the same form as one that transforms from a stationary to a rotating $dq0$ reference-frame. The transformation between two rotating $dq0$ frames is equivalent to this thesis' $\alpha\beta 0$ to $dq0$ transformation. Eq. (2.5) is used to derive this transformation, whereas the "transformation between reference-frames" is derived in an alternative manner, using matrix multiplication: see section 3.10 of [2].

The $\alpha\beta 0$ to $dq0$ transformation can be geometrically interpreted in $\mathbb{R}^3$ as a pure rotation about the 0-axis by a specified angle θ_{ref}. Fig. 3-5 illustrates the axes and vector transformation locus diagrams for the $\alpha\beta 0$ to $dq0$ transformation.

Fig. 3-5a is the axes transformation where the $\alpha\beta 0$ axes are rotated counterclockwise (CCW) about the 0-axis by an angle θ_{ref}. It is helpful to visualise the motion of the axes and vectors to understand the $\alpha\beta 0$ to $dq0$ transformation. Balanced systems have a Cartesian vector $\overrightarrow{v_{\alpha\beta 0}}$ that lies in the $\alpha\beta$-plane and rotates CCW about the

0-axis at speed ω. Note that $\overrightarrow{v_{\alpha\beta 0}}$ has an arbitrary angle θ_0 with respect to the α-axis ($\theta_0 = \omega t + \phi_0$). The $\alpha\beta 0$ axes are stationary and θ_0 increases with time.

The $dq0$ axes of Fig. 3-5a are not stationary, unlike the $\alpha\beta 0$ axes. These $dq0$ axes rotate CCW about the 0-axis at an angle $\theta_{ref} = \omega_{ref}\, t + \phi_{ref}$. $\overrightarrow{v_{dq0}}$ is the Cartesian vector referenced to $dq0$ coordinates. If $\omega_{ref} = \omega$ then $\overrightarrow{v_{dq0}}$ will have v_d and v_q components which appear constant as the $dq0$ axes are rotating at the same speed as the Cartesian vector $\overrightarrow{v_{dq0}}$. This case is illustrated by condition (i) of Fig. 2-2.

Fig. 3-5b is the vector transformation, where the axes are fixed and the Cartesian vector $\overrightarrow{v_{\alpha\beta 0}}$ is rotated clockwise (CW) about the 0-axis by an angle θ_{ref}. Thus, the vector has a net CCW angle of $\theta_0 - \theta_{ref}$ relative to the d-axis. $\overrightarrow{v_{\alpha\beta 0}}$ is rotating CCW at an angular velocity ω when referenced to the $\alpha\beta 0$ axes. When referenced to the $dq0$ axes, the vector $\overrightarrow{v_{dq0}}$ has a CCW angular velocity of $\omega - \omega_{ref}$. If $\omega_{ref} = \omega$ then $\overrightarrow{v_{dq0}}$ will appear stationary on the $dq0$ axes.

$$\overrightarrow{v_{dq0}} = T_{dq0}\,(\overrightarrow{v_{\alpha\beta 0}}) = \boldsymbol{A_{dq0}}\overrightarrow{v_{\alpha\beta 0}} \tag{3.13}$$

The matrix $\boldsymbol{A_{dq0}}$ in Eq. (3.13) is found using Eq. (2.5). T_{dq0} is applied to each basis vector $\{\hat{\mathbf{e}}_\alpha, \hat{\mathbf{e}}_\beta, \hat{\mathbf{e}}_0\}$ as shown in Fig. 3-6. T_{dq0} rotates the vectors $\hat{\mathbf{e}}_\alpha$ and $\hat{\mathbf{e}}_\beta$ CW about the 0-axis by θ_{ref}. The components of $T_{dq0}(\hat{\mathbf{e}}_\alpha)$ and $T_{dq0}(\hat{\mathbf{e}}_\beta)$ can be found using trigonometric relations.

$$T_{dq0}(\hat{\mathbf{e}}_\alpha) = \begin{bmatrix}\cos\theta & -\sin\theta & 0\end{bmatrix}^\intercal \tag{3.14}$$

$$T_{dq0}(\hat{\mathbf{e}}_\beta) = \begin{bmatrix}\sin\theta & \cos\theta & 0\end{bmatrix}^\intercal \tag{3.15}$$

Fig. 3-6 shows how $\hat{\mathbf{e}}_0$ is preserved under T_{dq0}.

$$T_{dq0}(\hat{\mathbf{e}}_0) = \begin{bmatrix}0 & 0 & 1\end{bmatrix}^\intercal \tag{3.16}$$

The three transformed unit vectors given by Eq. (3.14), Eq. (3.15) and Eq. (3.16) are combined with Eq. (2.5) to find $\boldsymbol{A_{dq0}}$. The inverse transformation is found readily

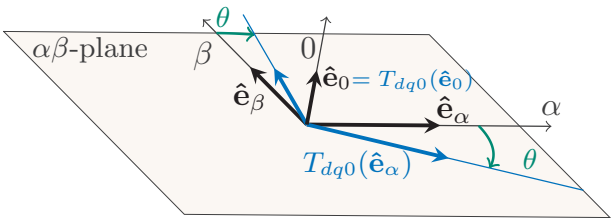

Figure 3-6: Geometric $\alpha\beta 0$ to $dq0$ derivation : (i) rotate $\hat{\mathbf{e}}_\alpha$ CW about 0-axis by θ_{ref} (ii) rotate $\hat{\mathbf{e}}_\beta$ CW about 0-axis by θ_{ref} (iii) preserve $\hat{\mathbf{e}}_0$ under T_{dq0}. Note: This figure uses the vector transformation perspective shown in Fig. 3-5b. This perspective highlights that the unit vectors rotate CW. While the axis transformation perspective in Fig. 3-5a has a CCW rotation of axes.

as the matrix is orthogonal ($\boldsymbol{A_{dq0}}^{\intercal} = \boldsymbol{A_{dq0}^{-1}}$).

$$\boldsymbol{A_{dq0}} = \begin{bmatrix} \cos\theta & \sin\theta & 0 \\ -\sin\theta & \cos\theta & 0 \\ 0 & 0 & 1 \end{bmatrix} \tag{3.17}$$

3.2.2 Power-Invariant Park Transformation Derivation

Park's transformation is derived utilising the relationships between the transformations in Fig. 2-1. The Park transformation is decomposed into the Clarke and $\alpha\beta 0$ to $dq0$ transformations in Eq. (3.18).

$$\overrightarrow{v_{dq0}} = T_{dq0}\left(T_c\left(\overrightarrow{v_{abc}}\right)\right) = \boldsymbol{A_{dq0}}\boldsymbol{A_c}\overrightarrow{v_{abc}} = \boldsymbol{A_p}\overrightarrow{v_{abc}} \tag{3.18}$$

The power-invariant Park transformation is constructed using the power-invariant Clarke transformation of Eq. (3.8) and the $\alpha\beta 0$ to $dq0$ transformation in Eq. (3.17). Please refer to Section 3.1.1 for a comprehensive derivation of the power-invariant Clarke transformation.

$$\boldsymbol{A_p} = \boldsymbol{A_{dq0}}\boldsymbol{A_c} = \boldsymbol{A_{dq0}}\sqrt{\frac{2}{3}}\begin{bmatrix} 1 & -\frac{1}{2} & -\frac{1}{2} \\ 0 & \frac{\sqrt{3}}{2} & -\frac{\sqrt{3}}{2} \\ \frac{1}{\sqrt{2}} & \frac{1}{\sqrt{2}} & \frac{1}{\sqrt{2}} \end{bmatrix}$$

$$\boldsymbol{A_p} = \sqrt{\frac{2}{3}} \begin{bmatrix} \cos\theta & \cos\left(\theta - \frac{2\pi}{3}\right) & \cos\left(\theta + \frac{2\pi}{3}\right) \\ -\sin\theta & -\sin\left(\theta - \frac{2\pi}{3}\right) & -\sin\left(\theta + \frac{2\pi}{3}\right) \\ \frac{1}{\sqrt{2}} & \frac{1}{\sqrt{2}} & \frac{1}{\sqrt{2}} \end{bmatrix} \tag{3.19}$$

3.2.3 Standard Park Transformation Derivation

The standard Park transformation can be determined in the same way as the power-invariant transformation using the relationships between the transformations (see Fig. 2-1) and Eq. (3.18). The difference is that the standard Clarke transformation of Eq. (3.12) is substituted for $\boldsymbol{A_c}$. $\boldsymbol{A_{dq0}}$ is given by Eq. (3.17). Please refer to Section 3.1.2 for a comprehensive derivation of the standard Clarke transformation.

$$\boldsymbol{A_p} = \boldsymbol{A_{dq0}}\boldsymbol{A_c} = \boldsymbol{A_{dq0}}\frac{2}{3}\begin{bmatrix} 1 & -\frac{1}{2} & -\frac{1}{2} \\ 0 & \frac{\sqrt{3}}{2} & -\frac{\sqrt{3}}{2} \\ \frac{1}{2} & \frac{1}{2} & \frac{1}{2} \end{bmatrix}$$

$$\boldsymbol{A_p} = \frac{2}{3} \begin{bmatrix} \cos\theta & \cos\left(\theta - \frac{2\pi}{3}\right) & \cos\left(\theta + \frac{2\pi}{3}\right) \\ -\sin\theta & -\sin\left(\theta - \frac{2\pi}{3}\right) & -\sin\left(\theta + \frac{2\pi}{3}\right) \\ \frac{1}{2} & \frac{1}{2} & \frac{1}{2} \end{bmatrix} \tag{3.20}$$

3.2.4 Standard Park Transformation Derivation: A Direct Geometric Approach

Previously in this thesis, the Park transformation was decoupled into two operations, as shown in Fig. 2-6. Understanding the Park transformation as two consecutive operations highlights the geometric relationship between the Clarke, Park and frame-to-frame transformations.

Alternatively, one can use the geometric approach to directly derive the transfor-

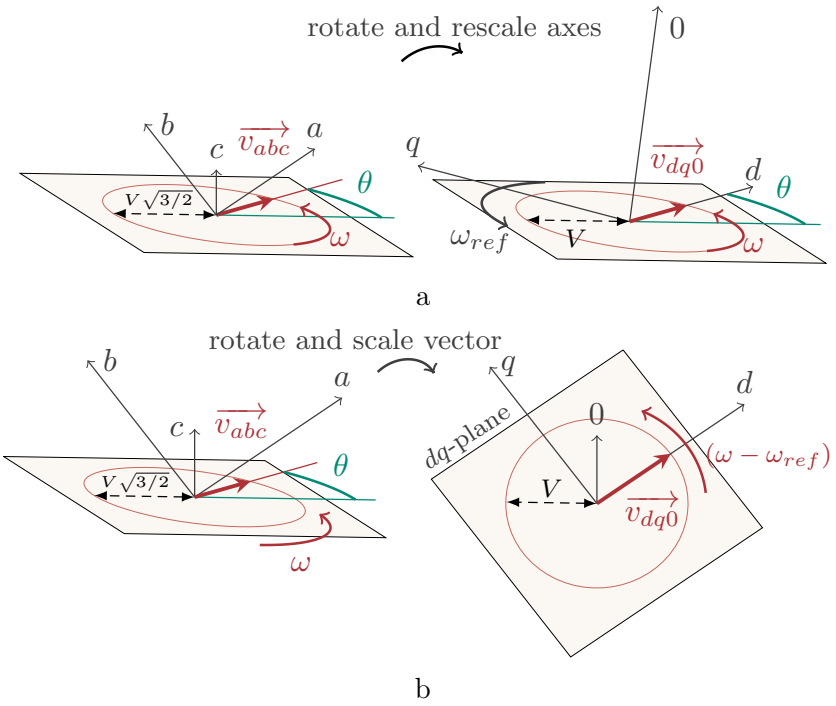

Figure 3-7: The standard (amplitude-invariant) Park transformation: (a) Axes transformation perspective: rotate the abc-axes such that the a-axis lines up with the vector v_{abc} at θ, and the b-axis also lies in the plane. Stretch the rotated ab-axes by $\sqrt{3/2}$ such that v_{dq0} has a length of V, when referenced to the dq-axes. The rotated and stretched ab-axes become the dq-axes respectively. The rotated c-axis becomes the 0-axis, and is stretched by $\sqrt{3}$ in order to agree with the definition of zero-sequence. (b) Vector transformation perspective: rotate the vector v_{abc} such that it lies in the ab-plane, and it rotates CCW about the 0-axis at a speed $\omega - \omega_{ref}$. Scale the rotated v_{abc} by $\sqrt{2/3}$ such that it has a length of V when referenced to the dq-plane. The 0-component of the vector v_{dq0} is scaled by $1/\sqrt{3}$ in order to agree with the definition of zero-sequence. Note: In both figures (a) and (b) the voltages are balanced, meaning the locus of v_{abc} is a circle of radius $V\sqrt{3/2}$.

mation from abc to $dq0$, without considering an intermediate $\alpha\beta0$ reference frame. In this section, this direct derivation is shown for the standard Park transformation using the approach outlined in Section 2.4 and given by Eq. (2.5). The power-invariant Park transformation can also be found directly using a similar approach.

Fig. 3-7 illustrates the standard abc to $dq0$ transformation. This is plotted for the case where the d-axis lines up with the vector $\overrightarrow{v_{dq0}}$. Refer to Fig. 3-5 for the case where the d-axis may not be in line with $\overrightarrow{v_{dq0}}$. Fig. 3-7a shows the axis transformation, where the axes can be seen rotating and stretching so that $\overrightarrow{v_{dq0}}$ traces out a circle of

radius V in the dq-plane.

Fig. 3-7b shows the same standard Park transformation from a different perspective. Instead of rotating and stretching the axes, the opposite steps are undertaken. The axes are fixed the vector is rotated and scaled so that $\overrightarrow{v_{dq0}}$ has a length of V and moves CCW about the 0-axis at a net speed of $\omega - \omega_{ref}$ relative to the dq-axes. $\overrightarrow{v_{dq0}}$ will appear stationary relative to the dq-axes, if Park's matrix is applied using a reference signal at the same frequency as the phase voltages ($\omega_{ref} = \omega$).

The inverse Park transformation T_p^{-1} is more convenient to derive geometrically than T_p (analogous to why T_c^{-1} was derived in Section 3.1). One can visualise how T_p^{-1} transforms vectors by reading Fig. 3-7 from right to left. The inverse transformation rotates the unit vectors $\hat{\mathbf{e}}_d$ and $\hat{\mathbf{e}}_q$ such that they lie in the plane of $\overrightarrow{v_{abc}}$. Thus, these transformed unit vectors $T_p^{-1}(\hat{\mathbf{e}}_d), T_p^{-1}(\hat{\mathbf{e}}_q)$ have a direction given by $\overrightarrow{v_{abc}}$ at angles of θ and $\theta + \pi/2$ respectively. Whereas T_p rotates the abc unit vectors $\hat{\mathbf{e}}_a, \hat{\mathbf{e}}_b, \hat{\mathbf{e}}_c$ to a location that is inconvenient to determine.

Park's matrix is derived by applying Eq. (2.5), which requires finding all three transformed unit vectors. These three steps are shown graphically by Fig. 3-8, where each of the unit vectors $\hat{\mathbf{e}}_d, \hat{\mathbf{e}}_q, \hat{\mathbf{e}}_0$ are transformed under T_p^{-1}. Fig. 3-8a shows how $\hat{\mathbf{e}}_d$ is transformed under the inverse Park transformation. $\hat{\mathbf{e}}_d$ is rotated such that it lines up with $\overrightarrow{v_{abc}}$ at angle θ and stretched by $\sqrt{3/2}$.

$$T_p^{-1}(\hat{\mathbf{e}}_d) = \overrightarrow{v_{abc}}\Big|_{\substack{V=1 \\ \theta}} = \begin{bmatrix} V\cos\theta \\ V\cos\left(\theta - \frac{2\pi}{3}\right) \\ V\cos\left(\theta + \frac{2\pi}{3}\right) \end{bmatrix}\Bigg|_{\substack{V=1 \\ \theta}}$$

$$T_p^{-1}(\hat{\mathbf{e}}_d) = \begin{bmatrix} \cos\theta & \cos\left(\theta - \frac{2\pi}{3}\right) & \cos\left(\theta + \frac{2\pi}{3}\right) \end{bmatrix}^{\mathsf{T}} \tag{3.21}$$

Similarly, Fig. 3-8b shows that $\hat{\mathbf{e}}_q$ is rotated and stretched by $\sqrt{3/2}$ such that it

lines up with $\overrightarrow{v_{abc}}$ at angle $\theta + \pi/2$.

$$
\begin{aligned}
T_p^{-1}(\hat{\mathbf{e}}_q) &= \overrightarrow{v_{abc}}\Big|_{\substack{V=1 \\ \theta+\frac{\pi}{2}}} \\
&= \left[\cos\left(\theta+\tfrac{\pi}{2}\right) \quad \cos\left(\theta+\tfrac{\pi}{2}-\tfrac{2\pi}{3}\right) \quad \cos\left(\theta+\tfrac{\pi}{2}+\tfrac{2\pi}{3}\right)\right]^\intercal \\
&= \left[-\sin\left(\theta\right) \quad -\sin\left(\theta-\tfrac{2\pi}{3}\right) \quad -\sin\left(\theta+\tfrac{2\pi}{3}\right)\right]^\intercal
\end{aligned}
\tag{3.22}
$$

Fig. 3-8c explains how $\hat{\mathbf{e}}_0$ is transformed. It points perpendicular to the plane of the locus and is scaled by $\sqrt{3}$, in order to correspond to the definition of zero-sequence. Mathematically, $T_p^{-1}(\hat{\mathbf{e}}_0) = [1 \quad 1 \quad 1]^\intercal$ is found by taking the cross-product of the other two transformed unit vectors, and scaled by $\sqrt{3}$, similar to Eq. (3.11).

All three transformed unit vectors are combined using Eq. (2.5) to give the standard inverse Park transformation matrix. One can take the inverse of Eq. (3.23) to obtain the transformation from *abc* to *dq*0, which will result in Eq. (3.20).

$$
\boldsymbol{A_p^{-1}} = \begin{bmatrix} \cos\theta & -\sin\theta & 1 \\ \cos\left(\theta-\frac{2\pi}{3}\right) & -\sin\left(\theta-\frac{2\pi}{3}\right) & 1 \\ cos\left(\theta+\frac{2\pi}{3}\right) & -\sin\left(\theta+\frac{2\pi}{3}\right) & 1 \end{bmatrix}
\tag{3.23}
$$

3.3 A Geometric Perspective on Power Quality

Power quality refers to harmonics and unbalance - both of which exist in all practical systems to some degree. Symmetrical components and the phasor representation are some of the tools used to analyse unbalanced systems. This section proposes an alternative view on power quality: a geometric interpretation. The locus diagram introduced in Section 2.5.1 is applied to three-phase quantities with harmonics or unbalanced phases.

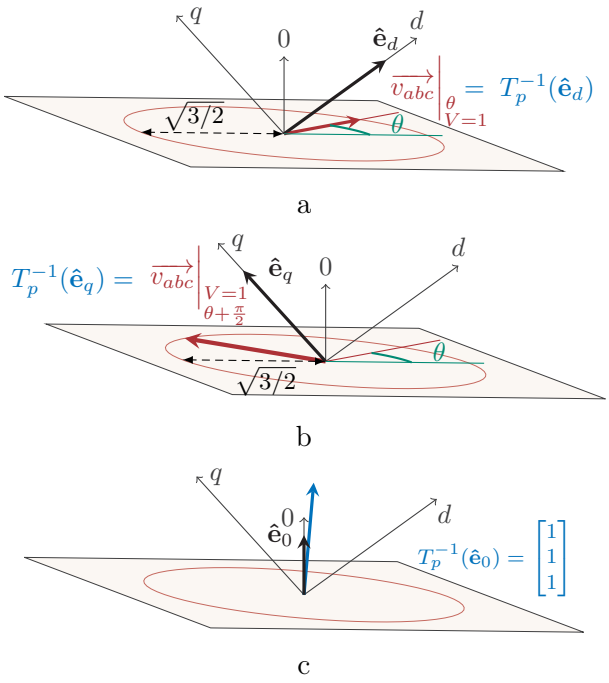

Figure 3-8: Geometric standard (amplitude-invariant) inverse Park derivation: (a) rotate $\hat{\mathbf{e}}_d$ to align with the vector v_{abc} at θ and stretch by $\sqrt{3/2}$ (b) rotate $\hat{\mathbf{e}}_q$ to align with the vector v_{abc} at $\theta + \frac{\pi}{2}$ and stretch by $\sqrt{3/2}$ (c) rotate $\hat{\mathbf{e}}_0$ perpendicular to the plane and stretch by $\sqrt{3}$. Note: This figure has stationary $dq0$-axes, as it uses the vector transformation perspective shown in Fig. 3-7b. This perspective highlights how the unit vectors stretch and rotate, which allows us to evaluate Eq. (2.5).

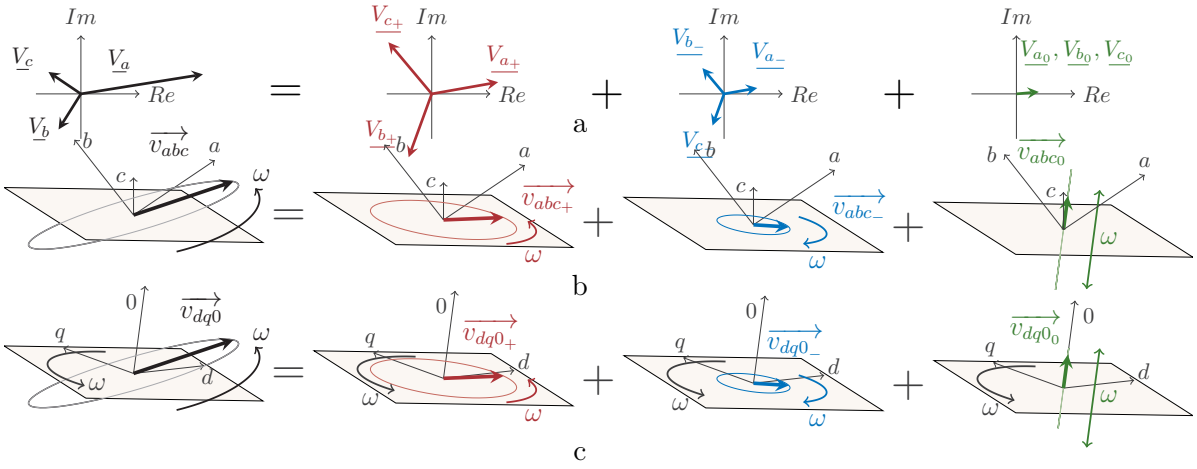

Figure 3-9: Symmetrical components applied to an unbalanced 3-phase system with no harmonics. (a) phasor diagrams (b) locus diagrams in *abc* coordinates (c) locus diagrams in rotating $dq0$ coordinates.

3.3.1 Unbalance: A Geometric Perspective

Phasor diagrams are commonly used to represent unbalanced three-phase quantities. Fig. 3-9a shows an example system that contains positive, negative and zero-sequence components, similar to condition (ii) of Fig. 2-2.

The locus diagrams for the unbalanced system of Fig. 3-9a are presented in *abc* coordinates in Fig. 3-9b. $\overrightarrow{v_{abc}}$ traces out an ellipse that lies outside the $\alpha\beta$-plane. This vector $\overrightarrow{v_{abc}}$ can be decomposed into three vectors corresponding to positive, negative and zero-sequence as shown in Fig. 3-9b. The positive and negative sequence loci lie in the $\alpha\beta$-plane, although their vectors rotate in opposite directions. The zero-sequence locus is a line-segment perpendicular to the $\alpha\beta$-plane and is traced out by a pulsating zero vector.

Fig. 3-9b provides insights on how symmetrical components appear on locus diagrams. The locus of systems with purely positive and negative sequence will always lie in the $\alpha\beta$-plane. This can be shown by taking the span of the two vectors $\overrightarrow{v_{dq0_+}}$ and $\overrightarrow{v_{dq0_-}}$ which is always equal to the $\alpha\beta$-plane (assuming an instant in time where the vectors are not overlapping, in which case the span is a line). The locus of systems that contain zero-sequence will not lie in the $\alpha\beta$-plane.

Fig. 3-9c shows the locus diagrams of the unbalanced system in $dq0$ coordinates. In

this example, it is assumed that the $dq0$ axes are rotating at the same speed ω as the signal. The positive sequence vector in $dq0$ coordinates rotates in the same direction as the $dq0$ axes. Therefore, positive sequence d and q-components will appear as constant values. The negative sequence vector rotates in the opposite direction as the dq axes, and its d and q-components will thus appear as a 2^{nd} harmonic. Naturally, the zero-sequence component lies on the 0-axis.

3.3.2 Harmonics: A Geometric Perspective

Harmonics generate positive, negative and zero sequence components in an interesting pattern [34]. The positive sequence harmonics are 1^{st}, 4^{th}, 7^{th} and so on. The harmonics 2^{nd}, 5^{th} and 8^{th} etc appear as negative sequence. Triplen harmonics (3^{rd}, 6^{th}, 9^{th} etc.) appear as zero-sequence in the abc domain. The first three harmonics are illustrated in Fig. 3-10a.

The locus diagrams of Fig. 3-10b provide an intuitive means to understand how harmonics appear in $dq0$. The relative velocity of a vector and the $dq0$-axes determines the frequency of the harmonic in the $dq0$ frame. Positive sequence components rotate in the same direction as the $dq0$ axes. Thus, $\overrightarrow{v_{dq0_4}}$ and $\overrightarrow{v_{dq0_7}}$ have d and q-components containing the 3^{rd} and 6^{th} harmonics respectively. Negative sequence components appear faster relative to the $dq0$ axes, such that $\overrightarrow{v_{dq0_2}}$ and $\overrightarrow{v_{dq0_5}}$ have d and q-components with the 3^{rd} and 6^{th} harmonics respectively.

Finally, a single locus diagram can fully represent a signal containing harmonics. This is not possible with a phasor diagram. Fig. 3-11 shows an example similar to case (iii) of Fig. 2-2. The vector $\overrightarrow{v_{abc}}$ contains fundamental, 5^{th} and 7^{th} harmonics. Both harmonics appear as a 6^{th} harmonic in $dq0$ as given by the shape of the locus of Fig. 3-11, which has 6 lobes.

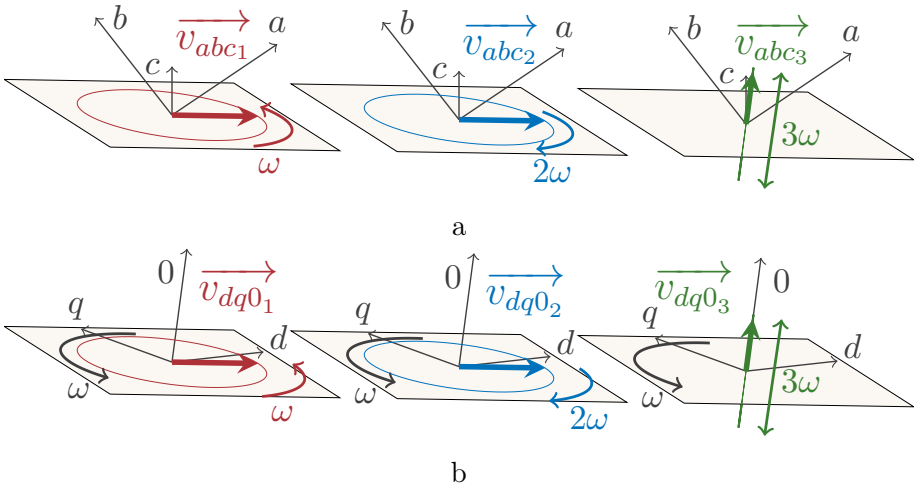

Figure 3-10: Locus diagrams of first three harmonics in: (a) *abc* coordinates (b) *dq*0 coordinates.

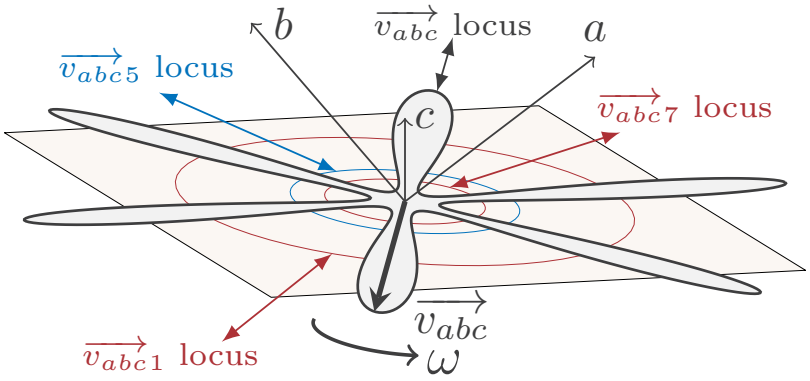

Figure 3-11: Locus diagram of a 3-phase system with 1st, 5th and 7th harmonics.

Part II

Stability Region Generation using Machine Learning

Chapter 4

Conditional Generative Adversarial Neural Networks applied to Stability Region Generation

This chapter provides an overview of Part II of this thesis. Decentralized generation in power systems is examined from the perspective of the system operator. System operators are faced with the challenge of maintaining stability despite significant changes in the power system, such as those caused by decentralization. Faults, changinging network topologies, power flows and fluctuating demand are changes which can adversly affect the stability of the power system. Stability region generation is proposed as a situational awareness tool that can assist the system operator in understanding and responding to system changes. In particular, as faults and other unexpected events occur this alters the set of stable control parameters (ie the stability region) an operator can choose from. Knowledge of this stability region can help operators understand the state of the system and suggest actions to take.

In this chapter, the need for situational awareness tools in power systems that are becoming more decentralized is discussed. Conditional Generative Adversarial Networks (cGANs) are proposed as a means to generate stability regions and previous work on using cGANs is explored. Following this, a framework for the application of cGANs to stability region generation is outlined in a sequence of steps. The train-

ing and hyperparameter tuning processes of cGANs can be challenging. To address this the chapter is concluded with a guide on how one can tune cGANs for their application.

4.1 Overview and Previous Work

Increasing the penetration of distributed generation leads to changing power flow patterns in power grids whereby the network configuration is liable to change. The ability of the system operators to respond to such real-time changes is essential for the reliable operation of the electricity grid. Therefore, situational awareness tools need to be developed in order for operators to make dynamic decisions.

Situational awareness is enabled as part of the centralized Supervisory Control and Data Acquisition (SCADA) system, which collects and presents real-time information to the system operator. As the system evolves over time, the operator responds by effecting changes on the system in the form of control modifications (e.g., enabling the PSS, operating circuit breakers, etc.). Using the SCADA system, the distributed generators in the system can be exploited to improve the reliability and availability of the grid. For example, a wind farm can be used to damp the rotor angle oscillations in a nearby synchronous generator [35]. At the distribution level, inverter-based generation can enable islanded operation in the event of grid failure. In either case, the SCADA functionality can be augmented with additional tools to better realize the potential of the distributed generation in improving the grid reliability. For instance, in the transmission case updating the wind farm controller gains, and in microgrids, changing the droop controller gains in response to network changes [36].

In most systems, larger values of controller gains (such as those of the wind-farm and droop controllers) improve the speed of response, but also tend to decrease the stability margin. The subset of the control parameter hyperspace where the system remains stable is termed as the *stability region*. Control parameters selected close to the stability region boundary yield an operating point with lower damping ratio, but better dynamic response [37]. Clearly, knowledge of the stability region is valuable in

resolving the trade-off between stability and dynamic performance.

Stability Region Generation (SRG) is the process of determining all control parameter sets that yields a stable system. There exist three approaches to SRG for a power system: (1) small-signal analysis, (2) time-domain simulation and (3) historical data from the physical system. Firstly, small-signal analysis has several issues when used to generate stability regions. Operators may not have a full analytical model available for the power system. If a model is available, the process involves the repeated computation of the eigenvalues of the system matrix for a wide range of control choices, making the process unscalable to large systems [38]. Secondly, time-domain simulations (based on numerical models of the system components) can be used to classify each point in the control parameter hyperspace. This is typically more time-intensive than the first case [39]. The third option is to select viable control parameters from historic data. This approach however may be overly conservative and moreover not adaptive to significant changes to the system configuration [40].

Model-free (numerical [41] as opposed to analytical) approaches using machine learning are being increasingly explored for stability studies in power systems. Typically, these entail the use of machine learning tools such as decision trees, support vector machines, etc. [40, 42–45] for online stability assessment, which seek to address the issues of computational burden of conventional security analysis methods. Deep learning techniques have also been recently proposed for power system stability studies. For instance, in [46, 47], convolutional neural networks (CNNs) are used to predict rotor angle instability by monitoring the voltage profiles. In [39], the results from existing time-domain simulations are leveraged by CNNs to infer stability conclusions for the early termination of the real-time stability assessment.

While the above works have focused on transient stability assessment, this thesis work extends the use of machine learning to determine the entire range of stable control parameters. Generative Adversarial Networks (GANs) are used as a stability region generation tool that would directly enable the system operator to influence the stability by adaptively tuning the control parameters in real-time. GANs are a machine learning tool that have primarily been applied to synthetic image generation. In

the context of power systems, GANs have been used to generate synthetic time-series data with the same probabilistic distribution as the training dataset. Some applications include probabilistic forecasting of sensory data [48], time-series data generation for wind [49, 50] and solar power [51], load data modeling [52], among others. GANs have also been used for generating missing data such as PMU measurements [53]. Some of these applications involve conditional GANs (cGANs), where a "conditional input" can be used to restrict the generated data to a particular class, for instance, weather data for *December*.

In this work, cGANs is used for stability region generation (SRG) by leveraging the conditional input as a feedback mechanism for the real-time system configuration. This framework has inherent stability assessment capability, and the stability region thus obtained is used to carry out the adaptive tuning of the control parameters. This enables the operator to maintain the system near the stability boundary, maximizing the dynamic performance while maintaining a sufficient stability margin. The proposed framework also allows the operator to flexibly impose limits on the stability margin and damping ratio, which makes it practicable. Further, the offline-trained GANs are shown to be scalable to power systems with a large number of control parameters.

4.2 The General Framework for cGANs Applied to Stability Region Generation (SRG)

This thesis uses a transmission case study that illustrates how the proposed cGANs-based situational awareness framework can facilitate operators in making dynamic decisions. The case study shows how a wind farm with energy storage can be exploited as a stabilizing resource for synchronous generation. Real-time control capabilities are required so as to effectively utilize this resource without compromising the stability.

From the context of this work, the function of the system operator is to update the control parameters of the power controllers to maintain stability as the system

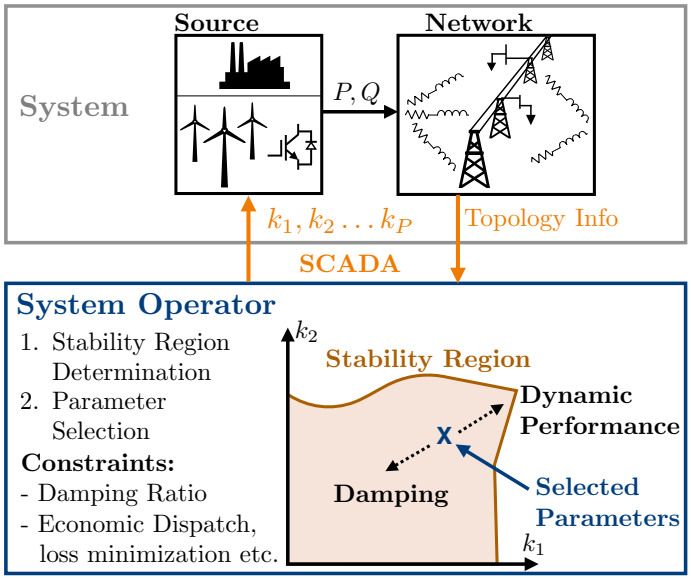

Figure 4-1: The proposed cGANs-based SRG framework for a generic power system.

configuration changes in real-time (see Fig. 4-1). The "system configuration" refers to the topology as well as loading, both of which are included in the power network model. The control process involves two steps: first, the calculation of the stability region, and second, the selection of suitable controller parameters from inside the stability region. Inherent to the parameter selection process is resolving the trade-off between the system damping (which is generally lower for higher controller gains) and the dynamic performance (higher for higher controller gains) [54].

4.2.1 The cGANs framework for Stability Region Generation

GANs are used to learn the probability distribution of a dataset. In the present context this corresponds to the probability distributions of the control parameters that constitute the stability region. In this subsection, the cGANs framework is formulated for the SRG application described in Fig. 4-1.

Fig. 4-2 illustrates the cGANs architecture during the training process. cGANs consist of two neural networks, referred to as the *generator* and the *discriminator*. Both networks use training data that is organised into categories, making up different conditional inputs. For example, datasets of people's faces could be conditioned

on things like age or gender. In the proposed framework where stability regions are generated for power systems, the conditional input u represents the network information. The system operator may already know stability regions for certian network topologies (eg $u_1 \dots u_n$ in Fig. 4-2), but not others. The set of known parameters for particular topologies makes up the training dataset.

The discriminator is a binary classifier which classifies its input as being either real or fake. The term *real* data in this application refers to data coming from an analytical model, a numerical model or experimental data. This real data is that which the system operator already has available and can use to train the cGANs. *Fake* data refers to data coming from the generator. This is data that is not provided by the sysem operator and is new data generated by the generator neural network. Depending on the value of y, the discriminator is fed either real data x or fake data $G(z|u)$. Note that the discriminator has a second input u, which is the conditional input (recall u is the network information in the proposed framework). The number of neurons per layer within a discriminator typically decreases between its input and output. The last layer is normally a sigmoid activation function which outputs a probability and is therefore a real number between 0 and 1. This probability is compared with a threshold of 0.5 to give $\hat{y}$, which is 1 if the discriminator classifies the data as being real and 0 if it thinks the data is false.

The generator takes both a conditional input u and an input vector z (also termed "noise vector" or "latent vector") and outputs $G(z|u)$ which is a fake sample for a particular conditional input. Initially, the generator's output will almost certainly not look anything like a real sample. However, after training the generator, its output may be indistinguishable from a real sample from the point of view of the discriminator.

The generator and discriminator have weights and biases denoted by θ_g and θ_d which are updated during the learning process. Learning is achieved via backpropagation where gradient descent is performed on the cost function and update the weights based on the direction that maximizes the change in gradient. Normally, training is completed for several cycles of the whole dataset where each single run through the training data is referred to as an *epoch*. The number of epochs required to train a

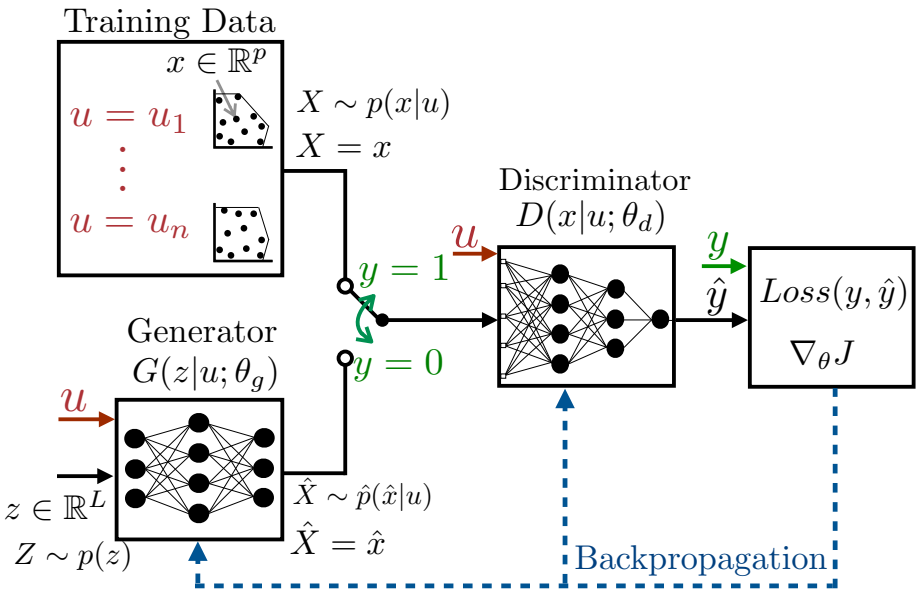

Figure 4-2: Conditional Generative Adversarial Neural Network

cGAN can vary significantly, but one typically stops training when the output of the discriminator's sigmoid is close to 0.5, meaning that it can no longer tell if a $G(z)$ is real or fake.

The overall problem formulation of using cGANs for stability region generation can be summarized into several steps. The remainder of this section elaborates on these steps.

Identify the conditional variable u

This is a vector of parameters that the system operator does not have control over as well as any constraints the operator wishes to impose. When changes occur in u, the SRG is re-triggered. Examples include network topology, line impedance and loading.

Identify the controller gains $x_1, x_2 \dots x_n$

Controller gains include parameters influencing the stability that can be changed in real-time. The notation $X \in \mathbb{R}^n$ in Fig. 4-2 denotes the continuous multivariate random variable that represents the controller gains while $x = [x_1\ x_2 \dots x_n]^\intercal$ refers to a particular sample of X and corresponds to each of the n control parameter taking on a particular set of values.

Let $p(x|u) = p(x_1, x_2 \dots x_p|u)$ represent the joint conditional probability distribution function (PDF) that the sample x lies in the stability region. This is intuitive as some choices of control parameters are more likely to appear in stable systems than others. Instead of attempting to obtain a closed-form expression for $p(x|u)$ which is often intractable, cGANs are trained to generate an estimate $\hat{p}(x|u)$ from which samples can be obtained. These samples are used to populate the estimated stability region corresponding to that conditional input u.

Generate the training data (samples of X)

The stability region is the subset of $\mathbb{R}^n$ which becomes the domain of X after training. Therefore, the samples x in the training dataset should be distributed over the entire theoretical stability region. This is done by sweeping each control parameter x_i, and determining the stability for each sample using an analytic model or numerical simulations. If stable, it is appended to the training dataset. This is repeated for different values of the conditional variable u.

Training

Training involves a game between the generator and discriminator. Referring to Fig. 4-2, when supplied with a noise variable z and a condition u, the generator is rewarded for producing samples $\hat{x} = G(z|u)$ that have a similar distribution to the training dataset. Whereas, the discriminator is rewarded for differentiating between the real samples from the training dataset and the fake samples produced by the generator. The discriminator outputs a binary variable $\hat{y} = D(x|u)$ that indicates its decision. The training is complete when the distribution of the generator output $\hat{p}(x|u)$ approaches that of the training dataset $p(x|u)$, whereby the discriminator can no longer distinguish between real and generated samples [55].

Stability Region Generation using cGANs

Given a real-time system configuration u, samples $\hat{x}$ obtained from the trained generator correspond to the PDF $\hat{p}(x|u)$, i.e., they lie in the desired stability region.

Table 4.1: cGANs Hyperparameters used in Case Study

Generator	Discriminator	Optimizer/ Learning Rate
5 Hidden layers: • Leaky ReLU ($\alpha = 0.2$) • Layer width=512 (all) • Dropout rate=0.5 • Batch size=32 Sigmoid output layer	3 Hidden layers: • Leaky ReLU ($\alpha = 0.2$) • Layer width=256, 128, 64 • Dropout rate=0.4 Sigmoid output layer	Adam $5e-5$

Therefore, the stability region can be generated by running the generator function several times, for randomly chosen latent vectors z.

4.2.2 cGANs hyperparameter selection

This section summarises the process of tuning the hyperparameters for the cGANs, based on lessons learned from working with the case study. The cGANs hyperparameters include the architecture of the discriminator and generator networks, and the factors influencing the training process including the optimizer and the batch normalization parameters. Since cGANs is a system of two competing networks viz. the generator and discriminator, the width and depth of each must be appropriately selected failing which the combined system fails to learn [56]. Specifically, the discriminator is made "weaker" than the generator by reducing its width or depth. Here, the width of all the generator layers were kept the same whereas the discriminator has decreasing nodes in higher layers as the eventual output is simply a binary output, i.e., real or fake. To find an adequate architecture, the size of both the networks are varied in tandem while maintaining similar relative sizing.

The first generator architecture tested was one with 4 hidden layers, with a width of 1024 nodes each. The output of the generator is a vector that lies in the space spanned by the stability region $\mathbb{R}^n$ where n is the number of control parameters. Therefore, the output layer of the generator contains n nodes. A sigmoid function is used for each of the n output nodes. Note that the output of a sigmoid is less than

1, and therefore this output needs to be re-scaled by some factor. The scaling factor used here is the same as the one used to normalize the training data. Each control parameter in the training data was normalized by the maximum observed value, so that the training data itself only contains values less than 1.

The discriminator was initially implemented with 3 hidden layers with respective widths of 1024, 512 and 1 nodes. Alternative implementations of the discriminator with wider layers were tested, and these wider layers in the discrmiinator were accompnaied by wider layers in the generator. The discriminator depth was increased if the width did not provide distinct improvement in the performance. At each stage, the efficacy of the cGANs-based SRG was evaluated using the following metrics: (a) the accuracy, defined by the fraction of the generated points that do lie in the theoretical stability region and (b) the coverage, defined by the spread of the generated points over the theoretical one. The final architectures selected are listed in Table 4.1.

The training process depends on the selected optimizer and the learning rate. The optimizer finds the weights in the hidden layers that minimize the cost function at each step while the size of the step is defined by the learning rate. A large learning rate can deter convergence while a small value will increase the computational burden. Gradient descent is a popular optimizer for GANs, and is considered in this work. For this case study a learning rate of $5e-5$ was sufficient; this also reduced the computational burden.

Furthermore, the activation function determines the output of each node through performing nonlinear transformation to the input such that the neural network can learn the complex relationships in the data. Here, differentiable activation functions were used along with the gradient descent optimizer, including Sigmoid, Tanh, ReLU and Leaky ReLU. The ReLU or "rectified linear unit" is an activation function $f(x) = max(0, x)$. Leaky ReLU refers to the activation function:

$$f(x) = \begin{cases} x & \text{if } x > 0, \\ \alpha x & \text{otherwise.} \end{cases} \tag{4.1}$$

From experimentation, Leaky ReLU is selected with $\alpha = 0.02$.

Finally, batch normalization [57] is executed after the activation function to improve the training process of GANs. The batch size is initially set to a small value to minimize the training time, and is increased if the loss function has a high amount of fluctuation. For the present application, a batch size of 32 was selected and the training process carried out for 50,000 epochs. In addition, dropout is included to reduce the risk of overfitting [58]. Dropout refers to temporarily excluding some neurons during the training process. A set of neurons are assigned a probability p of being used in each cycle of forward and back propagation. Through experiments, it was found that conducting the normalization after the dropout help to reduce the dropout rate. A dropout rate of $p = 0.4$ for the discriminator and 0.5 for the generator was found to be best.

Chapter 5

Case Study: Synchronous Machine Damping via Wind Farm

This chapter builds on the framework outlined in the previous chapter, and applies cGANs to a practical system involving a poorly damped synchronous machine and a wind farm. The chapter begins with a detailed description of the case study. This is followed by a demonstration of cGANs being used for stability region generation. The results show the the proposed framework can indeed produce stability regions with high accuracy.

5.1 Case study Overview

In this section, a transmission system is used to show the application of cGANs for real-time control. The system (see Fig. 5-1(a)) consists of a power network fed by a synchronous generator and is connected to a larger network modeled by an infinite bus. A wind farm is interfaced to the system via a 5 km transmission line, which offsets the load on the synchronous generator and damps its rotor angle oscillations. The permanent magnet synchronous generator (PMSG) based wind farm contains energy storage, which provides additional power required by the damping controller during a rotor transient. The parameters of the system are listed in Appendix A.

The aim of the cGANs-based control is to tune the parameters of the wind farm

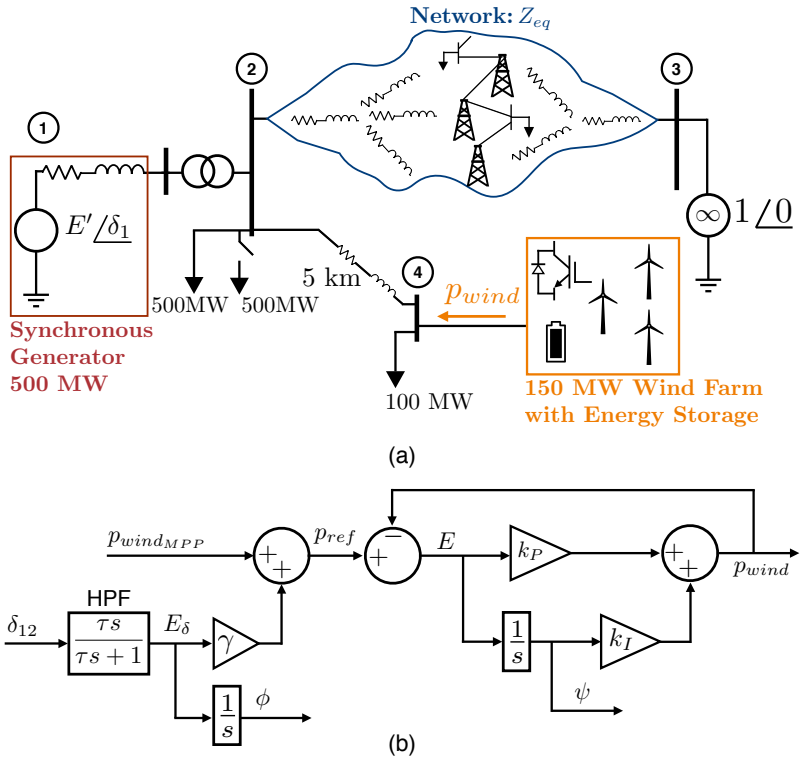

Figure 5-1: Transmission case study: (a) Wind farm with energy storage connected to network and a synchronous machine. (b) Control block diagram for mitigating power oscillations of the synchronous machine.

power controller in order to maintain stable operation as the network changes in real-time. Fig. 5-1(b) shows the controller for the wind farm, which enables the power output p_{wind} to track the reference p_{ref}. It is assumed that the plant dynamics of the power electronic interface are fast enough to be ignored - that is the p_{wind} commanded is instantaneously outputted by the power converter. The reference is tracked through the PI controller parameterized by the proportional and integral constants k_p and k_i. The total reference p_{ref} is made up of a DC reference $p_{windMPP}$ superimposed with a transient reference signal proportional to the oscillations of the synchronous machine. Damping is achieved by passing the voltage phase difference across nodes 1 and 2 in Fig. 5-1(a) through a high pass filter (HPF) with time constant τ, and amplified by a feedback gain γ.

The equations (5.1) to (5.4) describe the dynamics of the transmission case study. A simple per-unit classical model is used for the synchronous machine, whose states are per-unit frequency and rotor angle. The active damping control shown in Fig. 5-

Table 5.1: Transmission System Configurations Used For Training and Testing. See Appendix A for details on R/X ratio etc.

Training case	$\lvert Z_{eq}\rvert$ (Ω)	Test Case	$\lvert Z_{eq}\rvert$ (Ω)
Case-1	40	Case-5	60
Case-2	80	Case-6	100
Case-3	195	Case-7	155
Case-4	390	Case-8	230
		Case-9	290
		Case-10	350

1(b) has two states ψ (integrated total error) and ϕ (integrated transient error).

$$\Delta\dot{\omega} = \frac{1}{2H}\left(\Delta p_m - \Delta p_e - D\Delta\omega\right) \tag{5.1}$$

$$\Delta\dot{\delta_1} = \omega_B \Delta\omega \tag{5.2}$$

$$\Delta\dot{\psi} = \frac{-k_I}{k_P}\Delta\psi + \frac{1}{k_P}\Delta p_{wind} \tag{5.3}$$

$$\Delta\dot{\phi} = \frac{1}{\tau}\Delta\phi + \Delta\delta_{12} \tag{5.4}$$

Assuming small voltage deviations at transmission busses, the network algebraic equations can be expressed as:

$$\mathbf{\Delta P} = -\mathbf{B}\boldsymbol{\Delta\delta} \tag{5.5}$$

The dynamic equations are coupled with algebraic equations that relate the power flows and the angle at each bus. The reader is directed to Appendix A for details on how to combine the differential and algebraic equations for this case study. The system can now be written in linearized state-space form: $\Delta\dot{x} = \boldsymbol{A_1}\Delta x + \boldsymbol{A_2}\Delta u$, where the state vector is $\Delta x = [\Delta\omega\ \Delta\delta_1\ \Delta\psi\ \Delta\phi]^\intercal$ and the input vector is $\Delta u = [\Delta p_m\ \Delta p_{load}]^\intercal$.

$$\frac{d}{dt}\begin{bmatrix}\Delta\omega\\ \Delta\delta_1\\ \Delta\psi\\ \Delta\phi\end{bmatrix}=\begin{bmatrix}\frac{-D}{2H} & \frac{-m_1}{2H} & \frac{-m_2}{2H} & \frac{-m_3}{2H}\\ \omega_B & 0 & 0 & 0\\ 0 & \frac{c_1}{k_P} & (c_2-k_I)/k_P & \frac{c_3}{k_P}\\ 0 & (1-\beta_2) & -\beta_4 & -\left(\beta_3+\frac{1}{\tau}\right)\end{bmatrix}\begin{bmatrix}\Delta\omega\\ \Delta\delta_1\\ \Delta\psi\\ \Delta\phi\end{bmatrix}+\begin{bmatrix}\frac{1}{2H} & \frac{-m_4}{2H}\\ 0 & 0\\ 0 & \frac{c_4}{k_P}\\ 0 & -\beta_1\end{bmatrix}\begin{bmatrix}\Delta p_m\\ \Delta p_{load}\end{bmatrix} \tag{5.6}$$

5.2 cGANs-Based Stability Region Generation

The stability region for this system changes as the equivalent network impedance Z_{eq} changes. Therefore, to maintain stable operation, the system operator must monitor the stability region in real-time and ensure that the operating point remains stable with a good margin. To this end, cGANs are now adopted using the guidelines in Section 4.2.1. The stability region to be determined is a subset of the 4D hyperspace with each point characterized by the coordinates (k_p, k_i, τ, γ). The uncontrollable parameter that changes in real-time is Z_{eq}, which is taken as the (scalar) conditional input. The value of Z_{eq} can be estimated using the SCADA power flow data.

The training dataset consists of 40,000 evenly distributed samples $x = [k_p\ k_i\ \tau\ \gamma]^\intercal$ among four system configurations, viz., Cases 1, 2, 3 and 4 the details of which can be found in Table 5.1. Each "case" represents a particular system configuration, i.e., a value of the conditional input Z_{eq}.

Once trained, the performance of the cGANs is tested on Cases 5-10 from Table 5.1. For each case, the stability region is estimated by collating 1000 samples from the generator which is fed the appropriate conditional input (and random noise vector). The accuracy of the estimated stability region is verified using the model (Eq. (5.6)). The fraction of the generated points that are indeed stable is included in Fig. 5-2 as a measure of the cGANs accuracy; this exceeds 0.94 for all test cases.

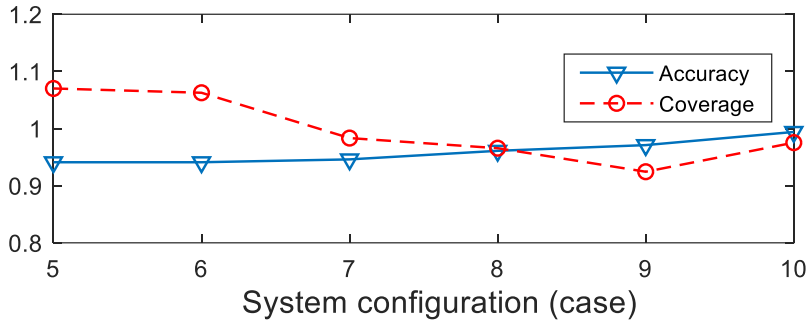

Figure 5-2: Accuracy and coverage of the cGANs-generated stability regions for the transmission case study. Accuracy refers to the proportion of points the generator correctly predicted a being stable. Coverage is the ratio of the area of the predicted stability region to the area of the theoretical region.

The coverage of the estimated stability region is defined as ratio of the volume of the estimated stability region to that of the theoretical stability region. Ideally, both the accuracy and coverage should be unity, indicating perfect accuracy. Note that the stability assessment and volume calculations are conducted using the model-based method in MATLAB. For the 2D stability regions shown, the area is used in lieu of volume, where coverage shown in Fig. 5-2 is calculated using the areas defined by the γ - k_p stability regions.

For verifying the shape of the estimated stability regions, they are plotted in Fig. 5-3 and superimposed on the theoretical stability regions for a few test cases. It is to be noted that while the actual stability region is a 4D hyperspace with a strong interdependence between the four control parameters, only selected 2D hyperplanes have been visualised. It can be observed that the cGANs is able to accurately estimate the entire stability region with good accuracy. If improved coverage is desired, more samples may be obtained from the generator. The stability region is also sensitive to changes in the conditional input, which demonstrates the adaptivity of the cGANs-based SRD.

Next, case study demonstrating the practical utility of the cGANs-based real-time SRD is considered. The transmission system is assumed to vary in real-time and sequentially go through the configurations Case- 7, 5, 10, 8 and 6. The cGANs is used for real-time SRD, subsequent to which the controller gains are tuned with the goal to maximize the dynamic performance while remaining in the stability region.

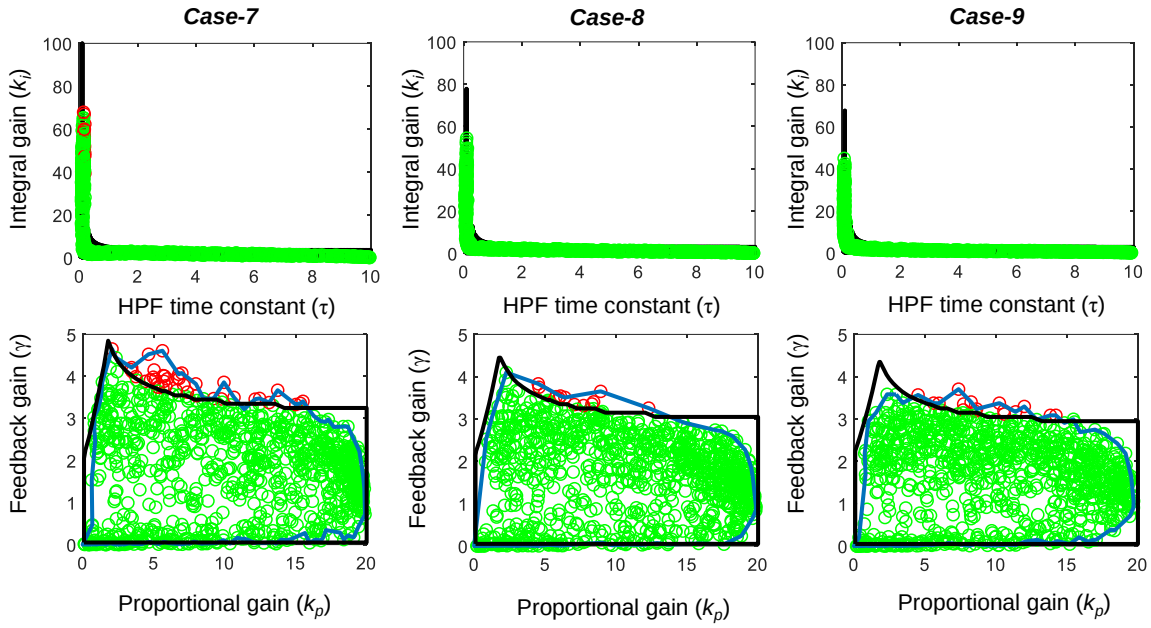

Figure 5-3: Stability regions obtained from cGANs for the transmission system for Cases 7, 8 and 9. Sample hyperplanes for the control parameters k_p, k_i, τ and γ are shown for different values of conditional input Z_{eq}, the effective impedance of the network between nodes 2 and 3. The theoretical stability region in each case is marked in black. The estimated stability region from cGANs is marked in blue. The points used to estimate the stability region are classified into green or red, based on whether or not they actually lie in the theoretical stability region.

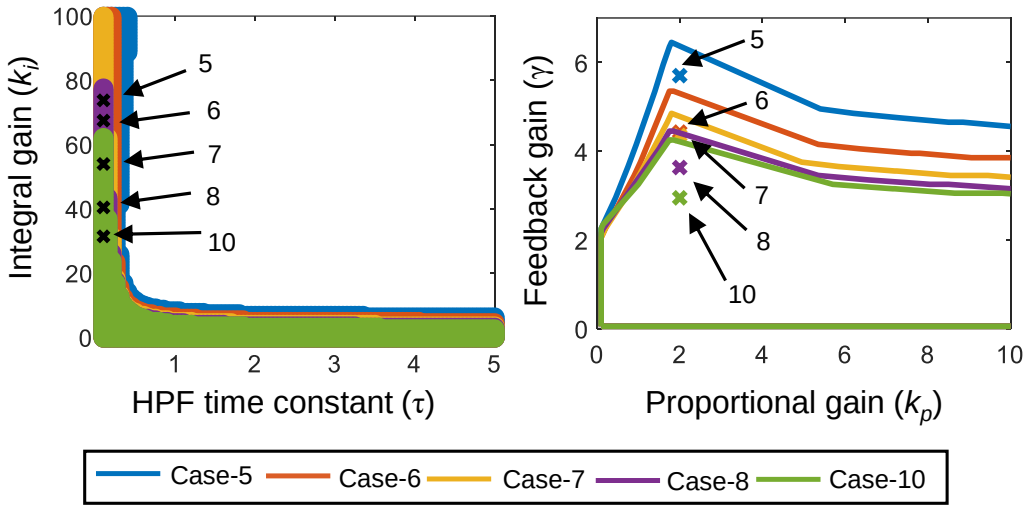

Figure 5-4: Theoretical wind farm active damping control stability regions for various system configurations. The operating point from the cGANs-based SRD is indicated by an $\times$. The selected operating points lie in the stability region with a robust stability margin.

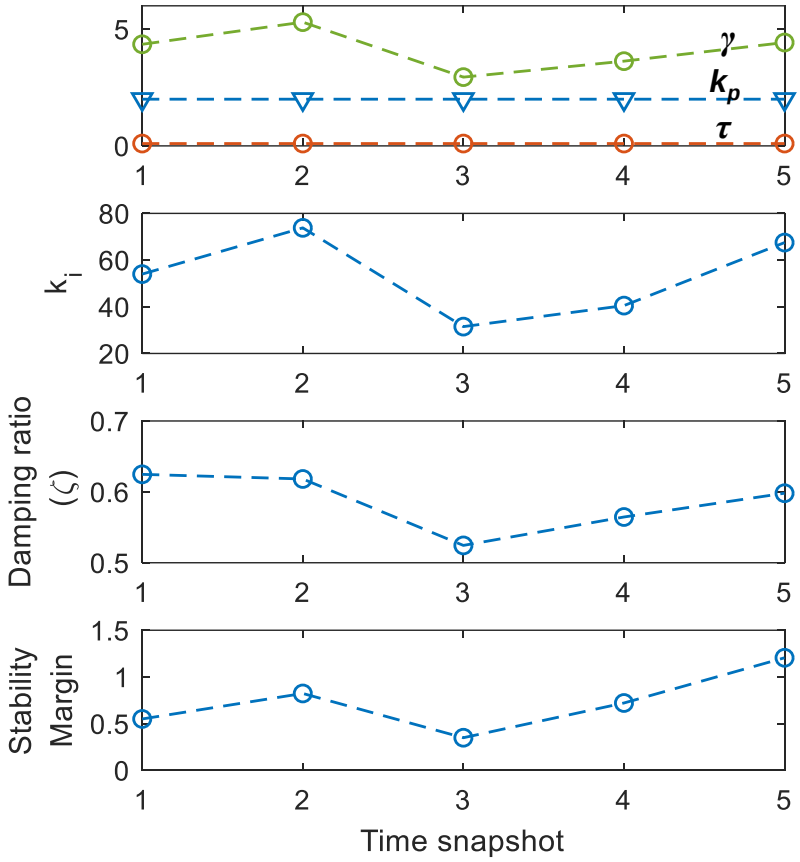

Figure 5-5: Plots of the tuned control parameters over 5 time snapshots. The system configuration for the snapshots in order are Case- 7, 5, 10, 8 and 6. For each case, the damping ratio and the stability margin are also plotted.

The theoretical stability regions for each case is shown in Fig. 5-4, along with the operating point selected from the estimated stability region. The operating point is selected as follows. The HPF parameter τ needs to be large enough to capture the rotor angle dynamics, while also lying inside the stability region. A value of 0.1 s was taken as it satisfied both criteria. Corresponding to this, $k_i = \alpha \max[k_i]|_{\tau=0.1}$ are selected, where the parameter α determines the distance of the selected operating point from the estimated stability boundary. Referring to the right-hand stability region in Fig. 5-4, the value of k_p is fixed at 2, as this is the approximate value at which the stability limit of γ is the highest. The maximization of the damping feedback gain γ is prioritized due to the main control objective being active damping. Then, depending on the conditional input, the stability limit is estimated and the operating point is chosen using: $\gamma = \alpha \max[\gamma]|_{k_p=2}$.

The operating points selected as above and the corresponding damping ratio (ζ) and stability margin for each time instance are shown in Fig. 5-5. The stability margin is the distance between the selected operating point (along normalized axes) and the nearest point on the stability boundary. The stability margin can be adjusted by changing the value of α, which embodies the trade-off between the stability margin and the damping ratio. It is observed that the damping ratio is positive for all system configurations, indicating that the system remains stable in real-time.

Chapter 6

Summary, Conclusions and Future Work

6.1 Thesis Summary

The goal of this thesis is to address challenges associated with the decentralization of generation in power systems. An increased proportion of renewable technologies in the form of solar photovoltaic and wind conversion systems will mean a higher proportion of inverters interfacing with the electricity network. As the number of inverters increases, the synchronous machine may not dominate power system generation as it has done in the past. Transformations such as the Park transformation were derived with the intention to analyse synchronous machines, yet somehow find uses in numerous other applications including three-phase inverter control. This motivates an alternative interpretation of reference-frames which is agnostic to a specific application. This problem is the focus of Part I of this thesis, which provides a solution in the form of a geometric interpretation of reference-frame theory.

Another aspect of decentralization is the increased variability of the system. Part II of this thesis examines the role of the system operator in maintaining stability, in the face of increased uncertainty due to decentralization. As the power system changes, the stable set of control parameters which make up the stability region also changes. Knowledge of how this set of parameters changes can facilitate the system

operator in making dynamic decisions. Generating these stability regions may be slow, inconvenient or dangerous depending on the approach taken. This motivates an alternative approach which can quickly generate an approximation of the stability region as the system changes.

6.2 Conclusions

In Part I it is shown that although the Clarke and Park transformations were originally derived to address challenges in specific problems, they can be derived in a more general manner. As each of these transformation are linear, one can exploit this linearity property and derive the matrices corresponding to each of the transformations by calculating how the transformation affects each of the standard basis unit vectors. This approach is applied to both the power-variant and the standard forms for each of the Clarke and Park transformations. The approach interprets each transformation as a combination of rotations and scalings in $\mathbb{R}^3$, and allows one to derive both the power-invariant and standard forms.

The geometric perspective is shown to have applications in power quality. Symmetrical components are found to be intimately related to the transformations. Insights regarding how unbalance and harmonics appear in the $dq0$ domain are uncovered using the geometric interpretation of reference-frame theory. Specifically, the reason for 2^{nd} harmonic appearing in the $dq0$ signals of an unbalanced signal stems from the fact that the $dq0$ axes rotate in the opposite direction to the Cartesian representation of the negative sequence component. Similar intuition explains why negative sequence harmonics appear faster in the $dq0$ domain. In addition, unlike the phasor diagram, a single locus diagram can fully represent a three-phase quantity with harmonics.

In Part II of this thesis, a novel framework for the real-time control of power systems is developed. It is validated (via a case study) that if a system operator were to know the underlying real-time stability region for a system, then they could make decisions as the systems changes. cGANs are presented as an alternative means to

generate stability regions. Through a simple case-study, the effectiveness of cGANs is demonstrated and the results for several test scenarios all confirm an accuracy exceeding 90 %. The coverage or spread of points in the generated stability region is also found to be quite good, in that points near the boundary are predicted. This coverage metric is calculated to be within 10% of the theoretical value.

6.3 Future Work

Part I of this thesis focuses on general results that apply to all three-phase systems. Therefore, there is much opportunity to investigate how the framework can be used to represent signals from physical experiments. One interesting problem would be to examine how poor sensor calibration (eg. offset or bias present in a voltage sensor) could affect the locus diagram corresponding to that measured signal. Beyond this, the intuition gained from the geometric framework could lead to new designs in active-power filtering and novel grid synchronization control (eg. phase-locked loops).

The main area of development for Part II would be to try to implement the proposed stability region generation using actual physical system data. This would require collaborating with system operators to find out what data is available, and what specific stability regions they might find useful or interesting. In the long-term, one could test the real-time stability region generation capabilities of the proposed method, by introducing a pilot version of the product to be used in line with traditional SCADA.

A problem with using physical system data is that most power systems are operated in a conservative manner. Thus, obtaining data of control parameter selections close to the stability boundary may be difficult. To address this, future work could investigate how to obtain points close to the stability boundary in a way that does not adversely affect the system. If this proves difficult, perhaps it is possible to augment the stability region data from the physical system with data from the numerical model.

Reliability is another area to investigate in future work. To address this, one

could try to embed some additional constraints on the stability region. For example, enabling the generated stability region to be altered based on a desired minimum damping-ratio.

Aside from numerical approaches, one could explore analytical approaches to stability region generation. Defining power system analytical models can be cumbersome depending on how detailed one needs their model to be. Model-order reduction approaches could make it easier to generate stability regions for larger systems, by only focusing on the most important control parameters.

Appendix A

Transmission Case Study Parameters

A.1 Parameters of the cGANs Case Study

The synchronous machine parameters are as follows: $H = 0.5$ s, $D = 0.5$, $\omega_{rated} = 2\pi 60$ rad/s.

The transmission network parameters are as follows: The R/X ratio of the network between nodes 2 and 3 is 0.0824 and the impedance of the line between nodes 2 and 4 is $(0.032 + j0.3883)\Omega$/km.

A.2 Small-Signal Model for the cGANs Case Study

The substitutions used in the system matrix $\boldsymbol{A_1}$ and the input matrix $\boldsymbol{A_2}$ are as follows:

$$\alpha_1 = \frac{-\gamma k_P}{\tau B_{44}\left(1 + k_P\right)} \tag{A.1}$$

$$\alpha_2 = \frac{\gamma k_P}{B_{44}\left(1 + k_P\right)} \tag{A.2}$$

$$\alpha_3 = \frac{-B_{42}}{B_{44}} - \frac{\gamma k_P}{B_{44}\left(1 + k_P\right)} \tag{A.3}$$

$$\alpha_4 = \frac{k_I}{B_{44}\left(1 + k_P\right)} \tag{A.4}$$

$$\beta_1 = \frac{1}{B_{22} + \alpha_3 B_{24}} \tag{A.5}$$

$$\beta_2 = -\frac{B_{21} + \alpha_2 B_{24}}{B_{22} + \alpha_3 B_{24}} \tag{A.6}$$

$$\beta_3 = -\frac{\alpha_1 B_{24}}{B_{22} + \alpha_3 B_{24}} \tag{A.7}$$

$$\beta_4 = -\frac{\alpha_4 B_{24}}{B_{22} + \alpha_3 B_{24}} \tag{A.8}$$

$$c_1 = \frac{\gamma k_P \left(1 - \beta_2\right)}{1 + k_P} \tag{A.9}$$

$$c_2 = \frac{\gamma k_P}{1 + k_P} \left(\frac{k_I}{\gamma k_P} - \beta_4 \right) \tag{A.10}$$

$$c_3 = \frac{\gamma k_P}{1 + k_P} \left(\frac{1}{\tau} + \beta_3 \right) \tag{A.11}$$

$$c_4 = \frac{-\gamma k_P \beta_1}{1 + k_P} \tag{A.12}$$

$$m_1 = -B_{11} - \beta_2 B_{12} \tag{A.13}$$

$$m_2 = -\beta_4 B_{12} \tag{A.14}$$

$$m_3 = -\beta_3 B_{12} \tag{A.15}$$

$$m_4 = -\beta_1 B_{12} \tag{A.16}$$

In the above equations, the terms B_{ii} represent the (i, i) elements of the susceptance matrix $\mathbf{B}$.

Appendix B

Summary of Transformations

Table B.1 summarises the standard and power-invariant forms of the Clarke and Park transformations. Note that there are many conventions for the direction of the d and q axes, with some even having a q-axis lagging the d-axis. This thesis follows the $dq0$ convention of Kundur and others in [25, 28] (see Table B.1). The angle θ is referenced with respect to the d-axis as shown in Fig. 2-4. There exists an alternative convention where the angle is referenced with respect to the q-axis. This convention ($qd0$) is used by Krause and others [2, 4].

Table B.2 shows the instantaneous real and reactive power calculations in each of the $\alpha\beta0$ and $dq0$ domains. We use the definition of instantaneous reactive power given by [59].

Table B.1: Summary of Transformations

	Standard (Amplitude-Invariant)	Power-Invariant
Clarke abc to $\alpha\beta 0$	$\frac{2}{3}\begin{bmatrix} 1 & -\frac{1}{2} & -\frac{1}{2} \\ 0 & \frac{\sqrt{3}}{2} & -\frac{\sqrt{3}}{2} \\ \frac{1}{2} & \frac{1}{2} & \frac{1}{2} \end{bmatrix}$	$\sqrt{\frac{2}{3}}\begin{bmatrix} 1 & -\frac{1}{2} & -\frac{1}{2} \\ 0 & \frac{\sqrt{3}}{2} & -\frac{\sqrt{3}}{2} \\ \frac{1}{\sqrt{2}} & \frac{1}{\sqrt{2}} & \frac{1}{\sqrt{2}} \end{bmatrix}$
Park abc to $dq0$	$\frac{2}{3}\begin{bmatrix} \cos(\theta) & \cos\left(\theta-\frac{2\pi}{3}\right) & \cos\left(\theta+\frac{2\pi}{3}\right) \\ -\sin(\theta) & -\sin\left(\theta-\frac{2\pi}{3}\right) & -\sin\left(\theta+\frac{2\pi}{3}\right) \\ \frac{1}{2} & \frac{1}{2} & \frac{1}{2} \end{bmatrix}$	$\sqrt{\frac{2}{3}}\begin{bmatrix} \cos(\theta) & \cos\left(\theta-\frac{2\pi}{3}\right) & \cos\left(\theta+\frac{2\pi}{3}\right) \\ -\sin(\theta) & -\sin\left(\theta-\frac{2\pi}{3}\right) & -\sin\left(\theta+\frac{2\pi}{3}\right) \\ \frac{1}{\sqrt{2}} & \frac{1}{\sqrt{2}} & \frac{1}{\sqrt{2}} \end{bmatrix}$
Inverse Clarke $\alpha\beta 0$ to abc	$\begin{bmatrix} 1 & 0 & 1 \\ -\frac{1}{2} & \frac{\sqrt{3}}{2} & 1 \\ -\frac{1}{2} & -\frac{\sqrt{3}}{2} & 1 \end{bmatrix}$	$\sqrt{\frac{2}{3}}\begin{bmatrix} 1 & 0 & \frac{1}{\sqrt{2}} \\ -\frac{1}{2} & \frac{\sqrt{3}}{2} & \frac{1}{\sqrt{2}} \\ -\frac{1}{2} & -\frac{\sqrt{3}}{2} & \frac{1}{\sqrt{2}} \end{bmatrix}$
Inverse Park $dq0$ to abc	$\begin{bmatrix} \cos(\theta) & -\sin(\theta) & 1 \\ \cos\left(\theta-\frac{2\pi}{3}\right) & -\sin\left(\theta-\frac{2\pi}{3}\right) & 1 \\ \cos\left(\theta+\frac{2\pi}{3}\right) & -\sin\left(\theta+\frac{2\pi}{3}\right) & 1 \end{bmatrix}$	$\sqrt{\frac{2}{3}}\begin{bmatrix} \cos(\theta) & -\sin(\theta) & \frac{1}{\sqrt{2}} \\ \cos\left(\theta-\frac{2\pi}{3}\right) & -\sin\left(\theta-\frac{2\pi}{3}\right) & \frac{1}{\sqrt{2}} \\ \cos\left(\theta+\frac{2\pi}{3}\right) & -\sin\left(\theta+\frac{2\pi}{3}\right) & \frac{1}{\sqrt{2}} \end{bmatrix}$

Table B.2: Summary of Instantaneous Power Calculations

	Standard (Amplitude-Invariant)	Power-Invariant
$\alpha\beta 0$	$p(t) = \frac{3}{2}\left(v_\alpha i_\alpha + v_\beta i_\beta + 2v_0 i_0\right)$	$p(t) = v_\alpha i_\alpha + v_\beta i_\beta + v_0 i_0$
	$q(t) = \frac{3}{2}\left(v_\beta i_\alpha - v_\alpha i_\beta\right)$	$q(t) = v_\beta i_\alpha - v_\alpha i_\beta$
$dq0$	$p(t) = \frac{3}{2}\left(v_d i_d + v_q i_q + 2v_0 i_0\right)$	$p(t) = v_d i_d + v_q i_q + v_0 i_0$
	$q(t) = \frac{3}{2}\left(v_q i_d - v_d i_q\right)$	$q(t) = v_q i_d - v_d i_q$

Bibliography

[1] Colm J O'Rourke, Mohammad M Qasim, Matthew R Overlin, and James L Kirtley. A geometric interpretation of reference frames and transformations: dq0, clarke, and park. *IEEE Transactions on Energy Conversion*, 34(4):2070–2083, 2019.

[2] Paul Krause, Oleg Wasynczuk, Scott D Sudhoff, and Steven Pekarek. *Analysis of electric machinery and drive systems*. John Wiley & Sons, 2013.

[3] Bimal K Bose. *Modern power electronics and AC drives*. Prentice Hall, 2002.

[4] Peter W Sauer and M A Pai. *Power system dynamics and stability*. Wiley-IEEE Press, 1998.

[5] Nagaraju Pogaku, Milan Prodanovic, and Timothy C Green. Modeling, analysis and testing of autonomous operation of an inverter-based microgrid. *IEEE Transactions on power electronics*, 22(2):613–625, 2007.

[6] Dmitry Baimel, Juri Belikov, Josep M Guerrero, and Yoash Levron. Dynamic modeling of networks, microgrids, and renewable sources in the dq0 reference frame: A survey. *IEEE Access*, 5:21323–21335, 2017.

[7] Adedayo Aderibole, Hatem H Zeineldin, Mohamed Shawky El-Moursi, Jimmy Chih-Hsien Peng, and Mohamed Al Hosani. Domain of stability characterization for hybrid microgrids considering different power sharing conditions. *IEEE Transactions on Energy Conversion*, 33(1):312–323, 2018.

[8] Jacob A Mueller and Jonathan W Kimball. An efficient method of determining operating points of droop-controlled microgrids. *IEEE Transactions on Energy Conversion*, 32(4):1432–1446, 2017.

[9] Natalia Kroutikova, CA Hernandez-Aramburo, and Timothy C Green. State-space model of grid-connected inverters under current control mode. *IET Electric Power Applications*, 1(3):329–338, 2007.

[10] Paolo Mattavelli. A closed-loop selective harmonic compensation for active filters. *IEEE Transactions on Industry Applications*, 37(1):81–89, 2001.

[11] Louis Gustaaf Stokvis. *Der Spannungsabfall des synchronen Drehstrom-Generators bei unsymmetrischer Belastung*. Dr. von R. Oldenbourg, 1912.

[12] Louis Gustaaf Stokvis. Analysis of unbalanced three-phase systems. *Electrical world*, 65:1111–1115, 1915.

[13] Charles L Fortescue. Method of symmetrical co-ordinates applied to the solution of polyphase networks. *Transactions of the American Institute of Electrical Engineers*, 37(2):1027–1140, 1918.

[14] Edith Clarke. Determination of voltages and currents during unbalanced faults. *General Electric Review*, 40(11):511–513, 1937.

[15] Edith Clarke. Problems solved by modified symmetrical components. *General Electric Review*, 41(11 and 12):488–449, 1938.

[16] Edith Clarke. *Circuit analysis of AC power systems*, volume 1. Wiley, 1943.

[17] AE Blondel. On the empirical theory of alternators. *L'Industrie Electrique*, 1899.

[18] André Blondel and Comfort Avery Adams. *Synchronous motors and converters: theory and methods of calculation and testing*. McGraw-Hill Book Company, 1913.

[19] Robert H Park. Two-reaction theory of synchronous machines generalized method of analysis-part I. *Transactions of the American Institute of Electrical Engineers*, 48(3):716–727, 1929.

[20] RE Doherty and CA Nickle. Synchronous machines I-an extension of blondel's two-reaction theory. *Transactions of the American Institute of Electrical Engineers*, 45:912–947, 1926.

[21] He C Stanley. An analysis of the induction machine. *Electrical Engineering*, 57 (12):751–757, 1938.

[22] Gabriel Kron. *Equivalent circuits of electric machinery*. J. Wiley & Sons, 1951.

[23] D. S. Brereton, D. G Lewis, and C. G. Young. Representation of induction-motor loads during power-system stability studies. *AIEE Trans. on PAS*, pages 451–460, 1957.

[24] Paul C Krause and CH Thomas. Simulation of symmetrical induction machinery. *IEEE transactions on power apparatus and systems*, 84(11):1038–1053, 1965.

[25] Prabha Kundur, Neal J Balu, and Mark G Lauby. *Power system stability and control*, volume 7. McGraw-hill New York, 1994.

[26] Paul C Krause, F Nozari, TL Skvarenina, and DW Olive. The theory of neglecting stator transients. *IEEE Transactions on Power Apparatus and Systems*, (1): 141–148, 1979.

[27] Charles Concordia. *Synchronous machines: theory and performance*. Wiley, 1951.

[28] Arthur Eugene Fitzgerald, Charles Kingsley, and Stephen D Umans. *Electric machinery*, volume 5. McGraw-Hill New York, 2003.

[29] TA Lipo. *A Cartesian vector approach to reference frame theory of AC machines*. Department of Electrical and Computer Engineering, University of Wisconsin-Madison, 1984.

[30] Richard Zhang, V Himamshu Prasad, Dushan Boroyevich, and Fred C Lee. Three-dimensional space vector modulation for four-leg voltage-source converters. *IEEE Transactions on power electronics*, 17(3):314–326, 2002.

[31] Slobodan Gataric. A polyphase cartesian vector approach to control of polyphase ac machines. In *Industry Applications Conference, 2000. Conference Record of the 2000 IEEE*, volume 3, pages 1648–1654. IEEE, 2000.

[32] A. A. Montanari and A. M. Gole. Enhanced instantaneous power theory for control of grid connected voltage sourced converters under unbalanced conditions. *IEEE Transactions on Power Electronics*, 32(8):6652–6660, 8 2017.

[33] Gilbert Strang. *Introduction to linear algebra*, volume 3. Wellesley-Cambridge Press Wellesley, MA, 1993.

[34] Parag Kanjiya, Vinod Khadkikar, and Mohamed Shawky El Moursi. A novel type-1 frequency-locked loop for fast detection of frequency and phase with improved stability margins. *IEEE Transactions on Power Electronics*, 31(3):2550–2561, 2016.

[35] Durga Gautam, Vijay Vittal, and Terry Harbour. Impact of increased penetration of dfig-based wind turbine generators on transient and small signal stability of power systems. *IEEE Trans. Power Syst.*, 24(3):1426–1434, 2009.

[36] Yun Zhang and Le Xie. Online dynamic security assessment of microgrid interconnections in smart distribution systems. *IEEE Trans. Power Syst.*, 30(6): 3246–3254, 2015.

[37] Yun Zhang, Le Xie, and Qifeng Ding. Interactive Control of Coupled Microgrids for Guaranteed System-Wide Small Signal Stability. *IEEE Trans. Smart Grid*, 7(2):1088–1096, 2016. ISSN 19493053. doi: 10.1109/TSG.2015.2495233.

[38] G. Raman, J. C.-H. Peng, and H. H. Zeineldin. Optimal damping recovery scheme for droop-controlled inverter-based microgrids. *IEEE Trans. Smart Grid*, pages 1–1, 2020.

[39] Rong Yan, Guangchao Geng, Quanyuan Jiang, and Yanglin Li. Fast transient stability batch assessment using cascaded convolutional neural networks. *IEEE Trans. Power Syst.*, 2019.

[40] Ruisheng Diao, Vijay Vittal, and Naim Logic. Design of a real-time security assessment tool for situational awareness enhancement in modern power systems. *IEEE Trans. Power Syst.*, 25(2):957–965, 2010. ISSN 08858950. doi: 10.1109/TPWRS.2009.2035507.

[41] Matthew Overlin, Colm O'Rourke, Po-Hsu Huang, and James Kirtley. A timing comparison of different fpga-accelerated load flow solvers. In *2019 IEEE PES Innovative Smart Grid Technologies Conference-Latin America (ISGT Latin America)*, pages 1–6. IEEE, 2019.

[42] I Kamwa, SR Samantaray, and Geza Joos. Development of rule-based classifiers for rapid stability assessment of wide-area post-disturbance records. *IEEE Trans. Power Syst.*, 24(1):258–270, 2009.

[43] Ce Zheng, Vuk Malbasa, and Mladen Kezunovic. Regression tree for stability margin prediction using synchrophasor measurements. *IEEE Trans. Power Syst.*, 28(2):1978–1987, 2012.

[44] Kunjin Chen, Jun Hu, and Jinliang He. Detection and classification of transmission line faults based on unsupervised feature learning and convolutional sparse autoencoder. *IEEE Trans. Smart Grid*, 9(3):1748–1758, 2016.

[45] Alfredo Vaccaro and Claudio A Cañizares. A knowledge-based framework for power flow and optimal power flow analyses. *IEEE Trans. Smart Grid*, 9(1): 230–239, 2016.

[46] Ankita Gupta, Gurunath Gurrala, and P. S. Sastry. An Online Power System Stability Monitoring System Using Convolutional Neural Networks. *IEEE Trans. Power Syst.*, 34(2):864–872, 2019. ISSN 08858950. doi: 10.1109/TPWRS.2018.2872505.

[47] Jinxiu Hou, Chang Xie, Tianyue Wang, Zhihong Yu, Ying Lü, and Hongyang Dai. Power system transient stability assessment based on voltage phasor and convolution neural network. *Proceedings - 2nd IEEE International Conference on Energy Internet, ICEI 2018*, pages 247–251, 2018. doi: 10.1109/ICEI.2018.00052.

[48] Alireza Koochali, Peter Schichtel, Andreas Dengel, and Sheraz Ahmed. Probabilistic forecasting of sensory data with generative adversarial networks–forgan. *IEEE Access*, 7:63868–63880, 2019.

[49] Yize Chen, Yishen Wang, Daniel Kirschen, and Baosen Zhang. Model-free renewable scenario generation using generative adversarial networks. *IEEE Trans. Power Syst.*, 33(3):3265–3275, 2018.

[50] Congmei Jiang, Yongfang Mao, Yi Chai, Mingbiao Yu, and Songbing Tao. Scenario generation for wind power using improved generative adversarial networks. *IEEE Access*, 6:62193–62203, 2018.

[51] Fei Wang, Zhanyao Zhang, Chun Liu, Yili Yu, Songling Pang, Neven Duić, Miadreza Shafie-Khah, and João PS Catalão. Generative adversarial networks and convolutional neural networks based weather classification model for day ahead short-term photovoltaic power forecasting. *Energy conversion and management*, 181:443–462, 2019.

[52] Yuxuan Gu, Qixin Chen, Kai Liu, Le Xie, and Chongqing Kang. Gan-based model for residential load generation considering typical consumption patterns. In *2019 IEEE Power & Energy Society Innovative Smart Grid Technologies Conference (ISGT)*, pages 1–5. IEEE, 2019.

[53] Chao Ren and Yan Xu. A fully data-driven method based on generative adversarial networks for power system dynamic security assessment with missing data. *IEEE Trans. Power Syst.*, 34(6):5044–5052, 2019.

[54] Petr Vorobev, Po-Hsu Huang, Mohamed Al Hosani, James L Kirtley, and Konstantin Turitsyn. High-fidelity model order reduction for microgrids stability assessment. *IEEE Transactions on Power Systems*, 33(1):874–887, 2017.

[55] Ian Goodfellow, Yoshua Bengio, and Aaron Courville. *Deep Learning*. MIT Press, 2016. `http://www.deeplearningbook.org`.

[56] Ian Goodfellow, Jean Pouget-Abadie, Mehdi Mirza, Bing Xu, David Warde-Farley, Sherjil Ozair, Aaron Courville, and Yoshua Bengio. Generative adversarial nets. In *Advances in neural information processing systems*, pages 2672–2680, 2014.

[57] Sergey Ioffe and Christian Szegedy. Batch normalization: Accelerating deep network training by reducing internal covariate shift. *arXiv preprint arXiv:1502.03167*, 2015.

[58] Nitish Srivastava, Geoffrey Hinton, Alex Krizhevsky, Ilya Sutskever, and Ruslan Salakhutdinov. Dropout: a simple way to prevent neural networks from overfitting. *The journal of machine learning research*, 15(1):1929–1958, 2014.

[59] Hirofumi Akagi, Edson Hirokazu Watanabe, and Mauricio Aredes. *Instantaneous power theory and applications to power conditioning*, volume 62. John Wiley & Sons, 2017.